SIMULATION AND ANALYSIS OF A LOW-POWER RADIO LINK FOR SENSOR NODE NETWORKS

by

Ulrich Georg Schuster

Memorandum No. UCB/ERL M02/36

3 December 2002

SIMULATION AND ANALYSIS OF A LOW-POWER RADIO LINK FOR SENSOR NODE NETWORKS

by

Ulrich Georg Schuster

Memorandum No. UCB/ERL M02/36

3 December 2002

ELECTRONICS RESEARCH LABORATORY

College of Engineering
University of California, Berkeley
94720

Simulation and Analysis of a Low–Power Radio Link for Sensor Node Networks

by Ulrich Georg Schuster

Research Project

Submitted to the Department of Electrical Engineering and Computer Sciences, University of California at Berkeley, in partial satisfaction of the requirements for the degree of **Master of Science, Plan II.**

Approval for the Report and Comprehensive Examination:

Committee:

Professor Jan M. Rabaey
Research Advisor

12/3/02
Date

* * * * * *

Professor Robert W. Brodersen
Second Reader

12/3/02
Date

Simulation and Analysis of a Low–Power Radio Link for Sensor Node Networks

by Ulrich Georg Schuster

Research Project

Submitted to the Department of Electrical Engineering and Computer Sciences, University of California at Berkeley, in partial satisfaction of the requirements for the degree of **Master of Science, Plan II.**

Approval for the Report and Comprehensive Examination:

Committee:

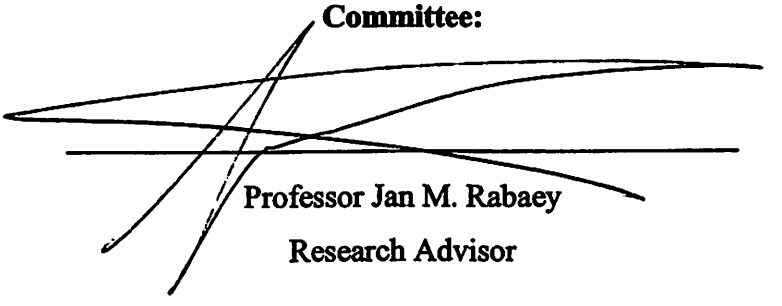

Professor Jan M. Rabaey

Research Advisor

12/3/02

Date

* * * * * *

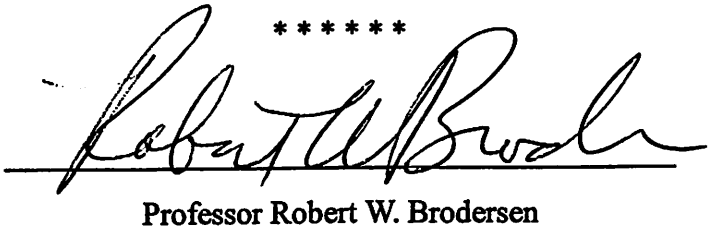

Professor Robert W. Brodersen

Second Reader

12/3/02

Date

Simulation and Analysis of a Low–Power Radio Link for Sensor Node Networks

by Ulrich Georg Schuster

Research Project

Submitted to the Department of Electrical Engineering and Computer Sciences, University of California at Berkeley, in partial satisfaction of the requirements for the degree of **Master of Science, Plan II.**

Approval for the Report and Comprehensive Examination:

Committee:

Professor Jan M. Rabaey
Research Advisor

12/3/02

Date

* * * * * *

Professor Robert W. Brodersen
Second Reader

12/3/02

Date

Simulation and Analysis of a Low–Power Radio Link for Sensor Node Networks

by Ulrich Georg Schuster

Research Project

Submitted to the Department of Electrical Engineering and Computer Sciences, University of California at Berkeley, in partial satisfaction of the requirements for the degree of **Master of Science, Plan II.**

Approval for the Report and Comprehensive Examination:

Committee:

Professor Jan M. Rabaey
Research Advisor

Date

* * * * * *

Professor Robert W. Brodersen
Second Reader

Date

Abstract

Wireless sensor node networks have the potential to become the next great driver application in the further development of wireless communication systems. Ubiquitous sensor nodes of small size, low cost and low power consumption form the enabling technology behind these future sensor networks. To achieve battery–independent operation through energy scavenging, all components of the system have to be optimized for ultra–low power consumption. This is especially critical for the analog components in the radio subsystem as traditional radios account for a large part of the overall energy budget of a wirèless appliance. To asses the performance of a radio link proposed by the PicoRadio RF group at the Berkeley Wireless Research Center, a simulation framework is needed that captures the behavior of the different analog building blocks. This simulation framework is described in detail; the various behavioral models of the analog components are derived and transformed into a baseband equivalent representation ready for simulation. Results of simulation runs are discussed and based on the simulation resutls, a simplified analytical model is developped, which can be used to study the effect of channel fading.

Acknowledgements

This work would not have been possible without the help encouragement and inspiration of all the people at the Berkeley Wireless Research Center. I would especially like to thank Professor Jan Rabaey for his support throughout the last semesters, for his ability to always provide the incentive to have the picture of the overall system in my mind while working on all the little details and for providing this great environment with people working in so many different fields yet cooperating and sharing their knowledge about the common project. The things I was able to learn here went far beyond the boundaries defined by the different disciplines. I would like to thank the people in the PicoRadio RF and baseband groups, Brian, Josie, Richard and Yuen–Hui for their help and patience, for designing all the circuits analyzed in this report and for being a great team.

Contents

List of Figures

List of Tables

1 Introduction

The modern living and working environment is mostly an artificial environment, engineered over the past centuries. In order to better adapt this environment to human needs like health and safety as well as to reduce negative ecological effects, one needs to add smartness to the mechanisms that control and regulate environmental functions e.g. the flow of traffic or the air conditioning in office buildings. Today most of the technology in the form of algorithms and computation power are available, the missing link is a cheap, reliable and simple way to collect the needed data. Wireless sensor networks are a key technology with the promise to achieve these goals and will play an important role in many fields in the near future. The possible applications are numerous, ranging from environmental monitoring for smart buildings, maintenance, agriculture and meteorology to consumer applications and education.

Key features of a wireless sensor network are *ad-hoc networking* such that no manual network setup and maintenance is necessary, *ultra-low power consumption* to increase the lifetime of the entire network [1] as well as *low cost* and *small form factor* to enable the ubiquitous use of hundreds of nodes in a network. The PicoRadio project [1] at the Berkeley Wireless Research Center is a systematic approach to develop a wireless sensor network having the characteristics mentioned above.

The physical layer in a network is responsible for providing a reliable point-to-point and point-to-multipoint link between neighboring sensor nodes. The special features of sensor applications imply rather low average data rates and short duty cycles of the radio. On the other hand the rigid power constraints necessitate a system level power optimization strategy with the goal of minimizing the total energy spent per successfully transmitted bit across the network, taking into account not only the transmitted energy over the channel but also all energy spent in analog and digital components of the radio. The goal of the PicoRadio project is an energy consumption on the order of several nanojoules per bit transmitted between two neighboring nodes.
Classical radio architectures like the superheterodyne receiver are optimized for high data rates and high spectral efficiency and are not particularly suited for the applications under investigation here. Thus new architectures are needed to fulfill the promise of an ultra-low-power radio link.

[1] Ideally the nodes would be powered solely by means of energy scavenging from the environment.

The optimization space is vast as it encompasses analog and digital circuit design parameters from circuit topology to layout issues, architectural considerations, communication theoretic parameters like the modulation scheme, error control coding and diversity strategies, networking aspects as end–to–end routing etc. No derived structure approach exists, where the resulting structure is the result of an optimization problem. The choice of a specific architecture, circuit topology etc. is based on heuristic argumentation and design experience. Furthermore, very little constraints are given in form of regulations the Project has to adhere to, resutling in an eveb larger design space. Hence it is important to provide a way to evaluate the impact of various analog and digital building blocks on system level performance parameters like the bit–error–rate (BER) and power consumption. The goal of this research project is the implementation of a system level simulation framework for the PicoRadio wireless point–to–point link and the integration of this simulation framework into the design process of the physical layer building blocks.

1.1 Overview

In section 2, I give a descriptive overview of approaches for ultra low power transceiver design and present the heuristic approach used to tackle the optimization problem. The envisioned architecture including the components under investigation is presented. Section 3 deals with the modeling of the components described in section 2 and the integration of these components into a complete transceiver model. The focus is on an appropriate description of the building blocks for use in a time domain simulation framework. The important parameters are identified and translated into a description convenient for implementation. In section 4, results from simulation runs are presented and building on these results, I further simplify the model, making it suitable for a semi–manual analysis. The important design tradeoffs are identified and implications for the system implementation derived.

2 Transceiver Architecture

The design of conventional cellular wireless communication systems is mainly concerned with achieving a high spectral efficiency (for applications in the licensed band) or high data rates (in

the unlicensed band). Mobile phone systems have to transmit over several kilometers, requiring transmit power levels on the order of one Watt. The dominant building block in terms of power consumption in these systems is the power amplifier, with a maximum efficiency around 60%. Hence, complex analog and digital circuitry can be used without adding too much to the overall power budget and enabling the use of efficient modulation schemes and sophisticated coding. Transceivers consume on the order of several hundred milliwatts while active and tens of microwatts when in sleep mode. Short range data systems like wireless local area networks transmit at lower power levels[2] and higher data rates. In these systems, the power consumption due to digital signal processing circuitry makes up a significant part of the overall power budget.

Compared to other wireless communication systems for data transmission, the requirements for sensor networks are somewhat different. The PicoRadio transceiver should be able to provide a reliable radio link over distances up to ten meters, where the current focus is on indoor environments. The duty cycle of the radio is low, the sensor nodes are in sleep mode most of the time. Hence the network is asynchronous and synchronization has to be performed each time before communication takes place between nodes. The typical data packets are short, less than a thousand bits.

2.1 Low Power Transceiver Architectures

Several standard transceiver architectures have evolved over the years, with the superheterodyne architecture still being the prevalent one. The image problem in the superhet necessitates off-chip filters; several energy–expensive conversion steps with one or two intermediate frequencies are used [2], rendering it less suited for an ultra low power, highly integrated implementation. In recent years the direct conversion concept has received considerable attention because its simplicity makes it a promising low power solution. It suffers however from such effects as dc offset, flicker noise and LO self–mixing. A description of the different architectures and a discussion of their characteristics from a power perspective can be found in the paper by Larson [3] and the dissertation by Yee [4].

Recently another interesting alternative has emerged in the form of ultra–wideband communication

[2]For example, in the unlicensed ISM band the overall transmitted power level is limited to 100mW in Europe.

systems. The pulse–position type modulation, lack of any frequency conversion and the fact that only very simple single bit analog to digital conversion is needed is very appealing from a power perspective while the large spreading factor and the resulting processing gain relax the channellization and interference management problems that arise in any wireless adhoc network because no frequency planning is possible in advance. Ultra–wideband systems are not considered here as a strong focus already exists at the Berkeley Wireless Research Center in parallel to the PicoRadio project [5]. The PicoRadio RF group instead focuses on the direct conversion principle, which will be the starting point for further investigations in the next sections.

2.1.1 General Considerations

To determine the right architectural choice, it is important to identify the main sources of power consumption in transceivers for the application at hand. A simple comparison between the power consumption of typical analog building blocks and the minimum average transmit power needed to achieve a given probability of error from a communication theory perspective will give some insight into where the biggest energy savings can be expected.

A simple link budget calculation is sufficient to give some intuition: Assuming an ideal linear receiver for the additive white Gaussian noise channel, the average transmitted power is (all values in dBm or dB resp.)

$$P_{TX} = G_{PL} - 174 + 10\log\frac{W}{\text{Hz}} + F + SNR_{min} \tag{2.1}$$

with the path loss G_{PL}, the equivalent noise bandwidth W, the receiver noise figure F and the signal to noise ratio SNR_{min} necessary to achieve the desired bit error rate. The noise floor of -174dBm assumes an ideal matched antenna with equivalent impedance of 50Ω. Assuming further an ideal brick wall filter and Nyquist transmit pulses, the data rate R can be related to the bandwidth as $R = 2W$. For a target bit error rate of 10^{-4} and binary modulation, the signal to noise ratio for optimal detection in additive white Gaussian noise is $SNR_{min} = 8.4$dB. If I further assume a path loss of 70 dB and a noise figure of 23 dB for the whole receiver chain as in the Bluetooth radio described by Haartsen [6], the average transmit power needed is $28.1\mu W$ or $-15.5dBm$. Dividing by the data rate R yields the energy per bit. In equation (2.1) this will cancel the equivalent noise bandwidth, rendering the expression independent of the data rate. Hence the

theoretically achievable energy per bit is 28.1 pJ.

This figure is quite low, an order of magnitude lower than the PicoRadio target of several nanojoule per bit. Unfortunately this does not imply that building low power radios is easy, because the link budget calculation only accounts for the energy actually transmitted. State of the art low noise amplifiers for 2G voice applications consume between 10 mW and 50mW according to the comparison of recently published numbers by Aparin [7]. Components for 2G/3G systems have generally high requirements in terms of linearity, sensitivity etc. which increase power consumption. Low power CMOS radios according to the Bluetooth specifications consume between 75mW and 180mW for the receiver and between 88mW and 130 mW for the transmitter [8] [9] [10]. A Bluetooth receiver front–end (without the IF section etc.) reported by Beffa [11] consumes 6.5 mW. Hence a single physically realizable component of the receiver chain is already enough to increase the power consumption by three orders of magnitude compared to the theoretical limit! This is a very important observation, indicating that most of the power is dissipated in the circuitry instead of being transmitted over the channel. A higher transmit power may thus indeed be beneficial because the specifications on the analog building blocks can be relaxed. For example a less stringent requirement on the LNA noise figure can lead to a significant decrease in bias current needed. But these possibly relaxed constraints on receiver specifications can also be used on an architectural level to radically simplify the transceiver architecture while e.g. using less efficient modulation schemes, allow for ISI etc.

A second observation is that for a given range of data rates, most analog blocks scale sub–linear with the data rate. Increasing the data rate while maintaining the same transmitted energy per bit again implies increasing the transmitted power. But now the energy per bit spent in most analog components decreases because the biasing stays constant. Limitations to this approach arise through components which scale linearly or super–linearly with the data rate like analog–to–digital converters, power amplifiers and symbol–rate–sensitive digital circuitry like the synchronization subsystem [12].

The above analysis is by no means rigorous, but it gives a hint for a suitable heuristic approach to the energy optimization problem at hand: reduce the radio to the simplest one possible with the least number of building blocks. With this radio, increase the data rate (and the transmit power) until the optimum for the chosen architecture is reached. This approach also implies that typical communication theoretic design considerations like modulation scheme and constellation size are

not fixed up front but will be determined by the capabilities of the radio.

2.1.2 Transmitter

Every transmitter has to perform some basic functions which cannot be further reduced. These are carrier generation[3], modulation, amplification and radiation.

To generate the carrier, an oscillator is needed which has to fulfill certain requirements like frequency accuracy and stability. Traditional oscillator designs can consume a significant amount of power. Low frequency oscillators locked to a crystal result in a very stable and accurate reference signal that needs to be upconverted in frequency to the desired value by means of a frequency synthesizer, a complex building block in itself. Oscillators directly operating at the carrier frequency consume less power, but are also less accurate due to the lack of high–Q RF filtering without bulky off–chip components.

The modulation of the carrier depends on the modulation scheme chosen, which will also be constrained by the demodulator. In general, the carrier can be modulated directly by influencing the operation of the oscillator or by means of a separate mixer. A mixer provides greater flexibility because the pulse generation can be separated from the upconversion process, allowing for accurate control of the spectral characteristics. Furthermore almost any modulation scheme can be used. Direct modulation has the advantage of being simple, while reducing the possible choices of modulation schemes. In accordance with the approach outlined in the previous section (2.1.1), the simplest component possible is used, a single directly modulated oscillator at the carrier frequency. This choice was greatly influenced by the availability of a new RF oscillator design by b. Otis [13] that employs high–Q micromachined filters for improved performance while keeping the power consumption as low as $300\mu W$.

The modulated signal around the carrier frequency has to be amplified to drive the antenna and produce the desired output power level. Hence the power amplifier has to operate at the carrier frequency. The key parameter for power amplifiers is their efficiency, defined as the ratio

[3]Ultra–wideband systems with a bandwidth starting at zero Hertz don't need a means to generate a carrier, the transmission pulses can be generated directly without the need for frequency conversion.

of power delivered to the antenna versus the overall amount of power consumed. To achieve a high efficiency, nonlinear amplifiers have to be used, which in turn preclude modulation schemes susceptible to waveform distortion like QPSK. Ideally the power amplifier would be co–designed with the antenna to minimize matching losses. Practical considerations however, like the available 50Ω test equipment, lead to a more traditional approach with a standard 50Ω load.

2.1.3 Receiver

Guided by the simplicity principle outlined in section 2.1.1, candidate architectures all belong to the class of direct conversion receivers. The benefits are fewer stages compared to heterodyne architectures, especially power-hungry mixers and image filters, while the drawbacks are dc offset problems for some schemes and flicker noise.

- The traditional direct conversion receiver uses one or two mixers, depending on the modulation scheme. A local oscillator, locked to the frequency of the incoming signal, drives the mixers. Besides the general problems of direct conversion receivers described above, the frequency synchronization may become prohibitive: In the analog domain, frequency synchronization is normally done using a phase locked loop, which itself is a complex building block and quite power hungry. The lock–in behavior is difficult to analyze, an in depth treatment is given by Stephens [14]. Moreover, for the very short packets (on the order of several hundred bits) of the PicoRadio system, the PLL lock–in time overhead increases the overall packet duration and thus counteracts the effort to keep the receiver active for the shortest amount of time possible. Instead of an all–analog PLL, digital carrier recovery can relax the requirements on the analog PLL by providing residual frequency synchronization in an open loop, decision directed approach. This approach promises shorter acquisition times at the cost of more involved digital signal processing as described by Meyr [12].

- A subsampling receiver relies on the frequency domain aliasing effect resulting from the signal being sampled below Nyquist rate [15]. The principle is depicted in figure 2.1. This concept can be extended to downconvert multiple channels at large frequency offsets as demonstrated by Akos [16]. Because all frequency bands at multiples of the sampling rate are downconverted to baseband, sharp RF filters are needed to prevent signals in these un-

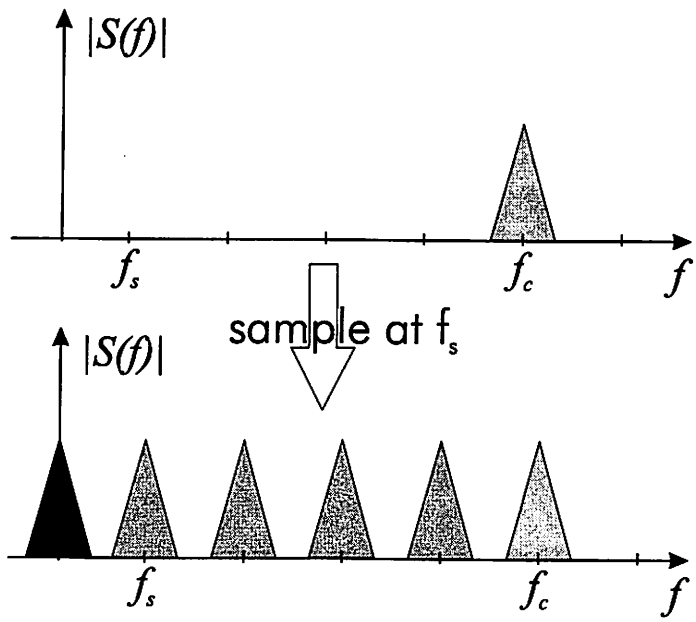

Figure 2.1: Subsampling Principle

wanted bands from reaching the sampler. In addition, any wideband noise entering the signal path after the filtering will be aliased, significantly increasing the baseband noise level, which is already high due to flicker noise. The flicker noise problem can be mitigated if the signal is not converted to baseband but to a very low IF instead, which can be processes further in the digital domain. The advantage of the subsampling approach is that no intermediate stages are needed, except for some RF amplification and filtering. This RF filtering is the crucial factor. RF filters with the necessary bandwidth are normally passive off–chip components, or require a large amount of RF amplification to overcome the insertion losses and the noise. In the above–cited paper by Akos [16], 100 dB of RF gain is needed, clearly not compatible with a low power design philosophy. Emerging new filter technologies such as RF MEMS seem to be promising alternatives.

- Envelope detection uses no local oscillator; instead the incoming signal is mixed with itself by means of some nonlinear element. The technique has been around for many years due to its appealing simplicity. Early vacuum tube radios used the envelope detection principle and even today simple AM receivers do. The nonlinearity introduces distortion and increases the noise bandwidth. As in the subsampling architecture, a sharp RF filter is needed to prevent adjacent signals from being downconverted to baseband, as no frequency discrimination is possible. Flicker noise is a major concern; a low IF solution as in the subsampling case is

not possible.

2.2 System Design

Given the various architectural options outlined above, it is very difficult to find an analytical formulation of the optimization problem resulting in the optimal architecture. Only modeling and simulation combined with actual hardware measurements seem to be a feasible approach. Therefore the PicoRadio RF group opted for the direct modulated transmitter and the envelope detector receiver as a starting point for further investigations. This choice was influenced by recent progress in micromachined RF filter technology, described later on in section 3.4.1, permitting low power RF oscillators and reasonably sharp front–end filters. Although for the subsampling approach the bandwidth provided is still too high to permit sampling close to the data rate. As the envelope detector is essentially an energy detector, only modulation schemes not depending on phase information are possible. These schemes are inherently wasteful of the degrees of freedom available for communication and therefore require a 3 dB higher signal to noise ratio for detection to achieve the same probability of error. This increase in transmitted energy however is surpassed by the energy savings possible due to the lack of a local oscillator at the receiver, a PLL and mixers.

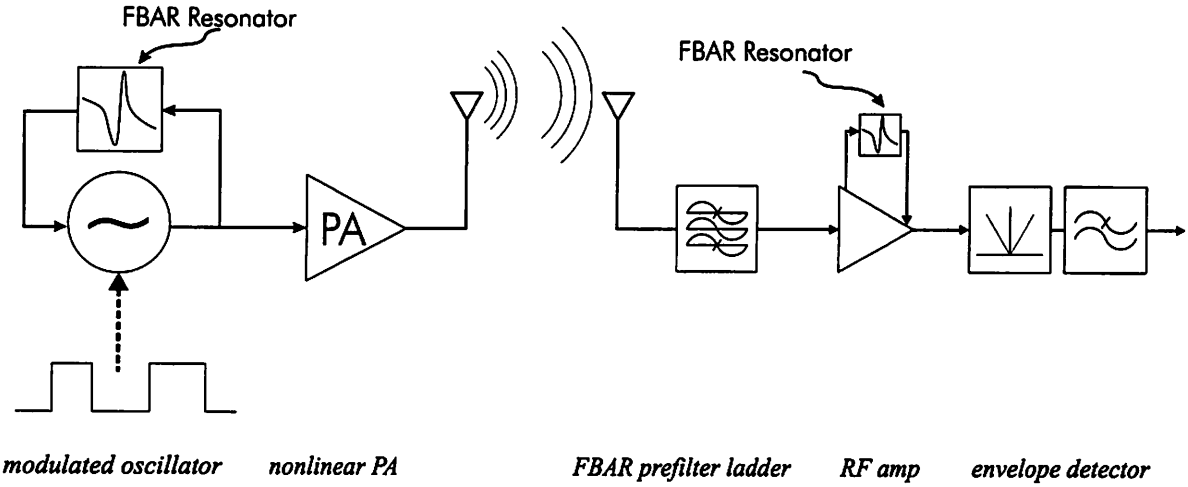

Figure 2.2: The Transceiver Chain

The overall transceiver architecture for a point–to–point link is depicted in figure 2.2. The oscillator is directly modulated by changing its bias current. It feeds into a nonlinear PA with high power–added efficiency. Micromachined resonators are incorporated into the PA design to

confine the output spectrum. The receiver consists of a wideband micromachined front–end filter, a RF gain stage with moderate requirements on the noise figure, an incorporated high–Q RF filter around the carrier and an envelope detector. The data rate is limited by the minimum startup time of the oscillator. Further pulse shaping can be accomplished by modulating the bias current, a possibly low power solution still under investigation. Detection of the transmitted signal can be performed either in the analog or digital domain.

3 Transceiver Modeling

The transceiver chain in figure 2.2 differs vastly from conventional architectures, for which powerful tools exist to analyze their performance. The differences are mainly due to two factors. First, the receiver is nonlinear, hence the transmitted pulses and the noise undergo nonlinear distortion that has to be taken into account. Second, the transmit pulse shape is not very well controlled by the designer. Several questions need to be answered:

- What is the performance that can be expected from the proposed architecture?
- What are the parameters having the strongest impact on the overall system performance and how can they be optimized to get the maximum marginal return?
- Is the premise of trading *communication energy* (i.e. energy per bit transmitted over the channel) for *implementation energy* (i.e. the overall energy needed in all components to transmit a bit) correct?

To answer the first two questions, a simulation framework incorporating the behavior of the analog building blocks can be used. Furthermore, a system level simulation is necessary in the design of the digital baseband part, because the synchronization and detection units depend on the actual received waveforms and noise. In the remainder of this chapter, I will describe such a simulation framework and derive the behavioral models for various components. The third question is very difficult to answer as no direct functional relation exists mapping a certain communication functionality (e.g. frequency conversion) into a specific circuit topology for a given technology. The

only possible method is thus to actually design and implement alternative architectures to compare them with the one discussed here.

3.1 Methodology

As outlined in section 2, the building blocks to be used in the transceiver chain under investigation differ significantly from the well understood canonical structure of a modulator producing pulses with a controlled spectrum, quasi–ideal frequency conversion through mixers, high–order filters and additive white Gaussian noise. The method adopted hereafter is to first model the channel end to end, including the analog circuits in the transmitter and the receiver. This model is then employed to assess the raw bit–error–rate as a performance measure using the simplest possible detector, i.e. symbol–by–symbol threshold detection.

3.1.1 Simulation Requirements and Setup

The channel and device effects studied in the simulation framework are mainly physical in nature. The simulation has to be able to capture them with enough fidelity to allow for system level analysis. A transient, waveform based model is needed to obtain enough information on pulse shapes, inter–symbol interference etc. To characterize the noise behavior, a Monte Carlo approach is necessary, averaging over the system response to various different sample paths. The simulation speed should be high enough to allow adequate exploration of the design space. This requirement is in conflict with the simulation bandwidth needed to accurately capture the effects of the filters used. A simulation on a digital computer is always *discrete time* in nature, hence the minimum simulation time step has to be much shorter than the smallest time constant of the system to be simulated, which again is directly related to the maximum bandwidth of components in the system.

Computation of the bit error rate by comparing the detector output with the transmitted bits and dividing the number of errors by the total number of transmitted bits is an estimator for the probability of error. To obtain a good estimate, a large number of transmitted bits have to be simulated. A measure for the estimator accuracy is the confidence interval of the estimate. Using the fact that the detector output is a binomial random variable, Jeruchim [17] computes the number

of errors that need to be observed for a given confidence interval and confidence level. For example, to obtain an estimate that lies within 30% (= confidence interval) of the true value with probability 0.95 (= confidence level), at least 40 errors have to be observed; for a bit error rate of 10^{-4}, the transmission of 400000 bits has to be simulated. To increase the quality of the estimate, the number of simulated bits has to be increased. The limiting factor is the simulation time. But modeling errors will always result in uncertainty about the simulation result, hence excessively tight constraints on the confidence interval and confidence level do not improve the accuracy of the description of the physical system but only the estimate of the system captured by the simulation framework. Hence the confidence interval defined above is a good compromise. For lower levels of transmit power, the number of observed errors increases significantly and hence the bounds on the estimate are tighter.

Although most issues concerning the modeling and implementation of the simulation framework are independent of the simulator used, the impact on execution time can be big. For this project, I used the SIMULINK/MATLAB environment. The ease of integration with existing blocks[4] comes at the price of a sometimes suboptimal execution speed. I will only refer to these implementation issues where the proper choice has a significant impact on the simulation performance. MATLAB was originally build around the EISPACK and LAPACK numerical libraries, which provide efficient implementations of commonly used vector/matrix operations. Standard iterations like `for`–loops on the contrary are inefficient. To access the fast linear algebra routines from within the SIMULINK model, the preferred simulation mode is *frame–based.* A frame consists of a sequence of time domain sample points according to simulation steps, but most operations described by the simulation blocks now operate on the whole frame instead of one sample at the time. This approach introduces extra latency, meaning that at the output of the transceiver chain, the signal will be delayed with respect to the corresponding input signal, a fact that has to be taken into accunt in calibrating the simulation as well as for simulations of subsequent digital baseband blocks.

[4]Especially blocks from existing work by Dennis Yee [4]

3.2 Transmitter

3.2.1 Pulse Generation

As discussed in section 2.1.2, the transmitter is basically a triggered oscillator that generates on–off keyed pulses, followed by a power amplifier. The power savings of this extremely simple architecture come at the price of design inflexibility of the modulation scheme and the pulse shape, both major design parameters in a conventional communication system. To asses the capabilities of this architecture, it is important to extract the main parameters describing the system, namely the transmit waveform.

The oscillator is triggered on and off by switching the bias current. Oscillation starts, the amplitude following an exponential envelope until the signal swing is large enough to drive the active device nonlinear. At this time, the startup transient slows down until an equilibrium is reached, defining the steady state oscillation amplitude. During the initial transient, the oscillation frequency changes from the frequency determined by the initial loop gain to the steady state oscillation frequency. Circuit simulations of the oscillator output are shown in figure 3.1. Two

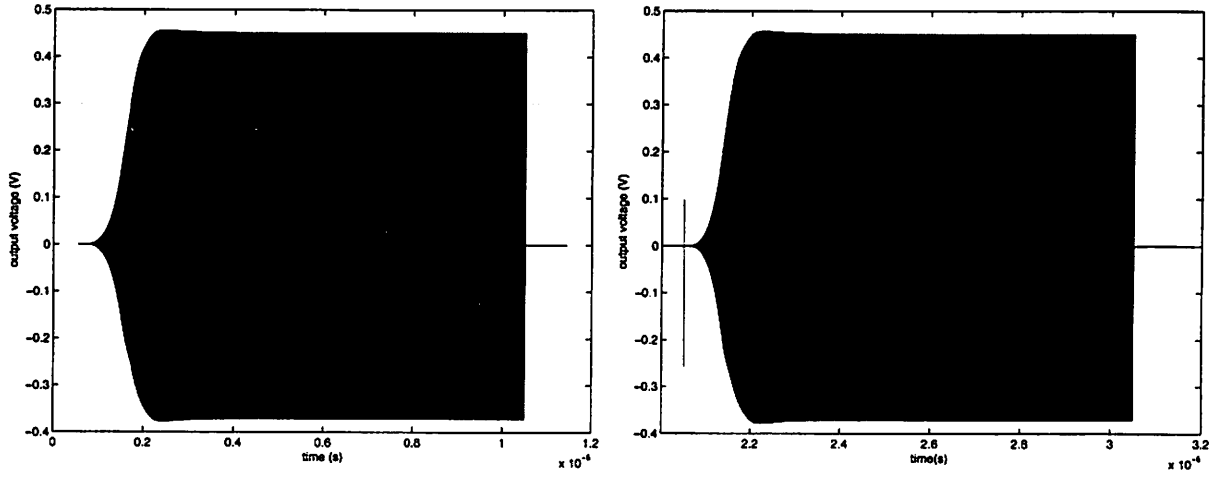

(a) Oscillator Output Voltage (b) Power Amplifier Output Voltage

Figure 3.1: Transmit Waveforms

important properties of the pulses can be observed: (1) the startup time of the oscillator is approximately 800ns. If the oscillator is combined with a power amplifier, this startup transient lasts

longer, approximately[5] 1.5μs. (2) The fall time is very rapid, due to the reduced quality factor (Q) of the oscillator loop when the bias current is turned off. The rising and falling transitions can be modified by either changing the circuit characteristics (initial loop gain, Q) or by modulating the bias current.

3.2.1.1 Behavioral Model The startup transient follows an exponential curve until the nonlinear behavior of the device characteristics dominates. A function which combines the effects of a positive and a negative exponential is the hyperbolic tangent, defined as

$$\tanh(x) = \frac{e^x - e^{-x}}{e^x + e^{-x}} \tag{3.1}$$

Curve–fitting this function to the simulated transmitter pulse given in figure 1(b) shows a good match, as seen in figure 2(a). The fit for the falling edge is not as good as for the rising edge, because upon reduction of the bias current, the quality factor (Q) degrades, resulting in a very fast decay. The harmonics introduced by the nonlinear operation of the power amplifier can be observed in figure 2(b); the waveform deviates substantially from an ideal sinusoid. The functional relation

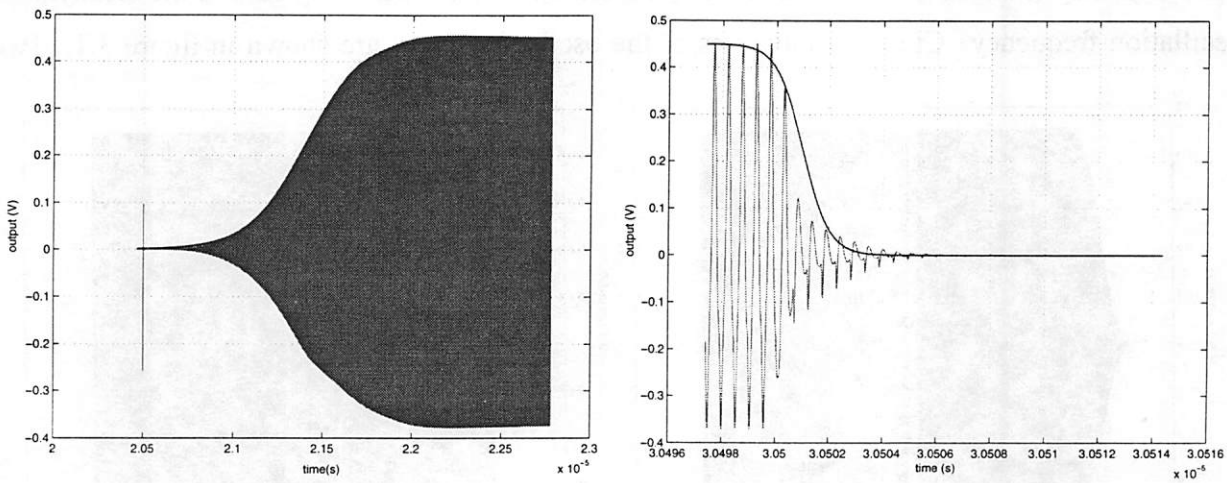

(a) rising edge (b) falling edge

Figure 3.2: Startup Transient at PA Output with Fitted Function.

achieving this match is given by

$$g(t) = \frac{0.45}{2}\left(\tanh\left(\left[t + \frac{T_s}{2}\right]a\right) - \tanh\left(\left[t - \frac{T_s}{2}\right]b\right)\right) \tag{3.2}$$

[5]This is a preliminary result, as the power amplifier used for the simulation has since been modified and will be fabricated soon

where T_s denotes the duration of the pulse measured form the midpoint of the rising and falling transient, $a = 3.1878 \times 10^6$ and $b = 1000 \times 10^6$ are the coefficients determining the rise and fall times, respectively. These results are still preliminary as they are based on circuit simulation of the first design draft of the transmitter, but the general modeling approach remains valid as the characteristic of the starting and decaying oscillator envelope will remain.

Important for the design of the communication system is the spectrum of the pulses. The Fourier Transform[6] of (3.2) is obtained using the transform pair as given by Bracewell [18]:

$$\tanh(\pi t) \longrightarrow \frac{-j}{\sinh(\pi f)} \tag{3.3}$$

Using the similarity theorem, the spectrum is

$$G(f) = \frac{0.45j\pi}{2}\left(\frac{e^{-j\pi f T_s}}{b\sinh\left(\frac{\pi^2 f}{b}\right)} - \frac{e^{j\pi f T_s}}{a\sinh\left(\frac{\pi^2 f}{a}\right)}\right) \tag{3.4}$$

For the special case of $a = b$ (symmetric pulses), equation (3.4) can be simplified yielding

$$G_{sym}(f) = 0.45\frac{\pi\sin(\pi f T_s)}{2a\sinh\left(\frac{\pi^2 f}{a}\right)} \tag{3.5}$$

For $f = 0$, equations (3.4) and (3.5) are not continuous. However, as in the definition of the *sinc* function, the discontinuity can be resolved by setting $G(0)$ equal to the limit for $f \longrightarrow 0$. For the values of a and b given above and $T_s = 100\mu s$, the analytic spectrum plot is given in figure 3.3. As can be observed, the magnitude spectrum closely resembles the one of a perfectly rectangular pulse. This is problematic as the excess bandwidth is large due to the slow decay (proportional to $1/f$) of the sinc function.

Next, the spectral variation versus the pulse–slope is examined. Figure 3.4 shows several symmetric pulses and their corresponding spectra. The parameter shown is the change in the slope as modeled by the parameter a in equation (3.5) with the reference being the extracted value. Only

[6]throughout this report, I use the following definition of the Fourier Integrals:

$$S(f) = \int_{-\infty}^{\infty} s(t)e^{-j2\pi ft}\mathrm{dt}$$
$$s(t) = \int_{-\infty}^{\infty} S(f)e^{j2\pi ft}\mathrm{df}$$

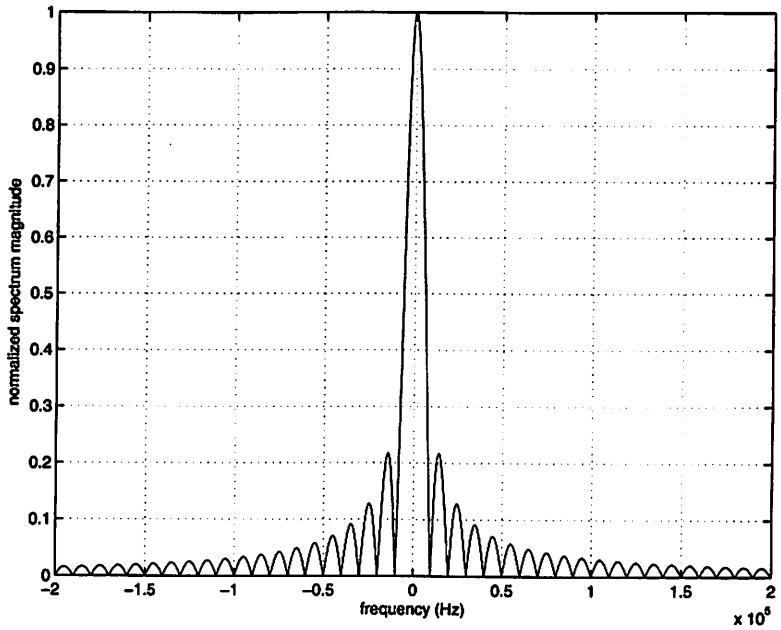

Figure 3.3: Normalized Spectrum of a Transmitter Pulse with $T_s = 100\mu s$

for pulses with very broad skirts does the spectrum show significantly more narrowband behavior. Experiments with the transmitter oscillator[7] showed that it is possible to influence the skirts of the pulses by modulating the bias current. As this increases the design flexibility, the impact will be evaluated simulating the performance of the system for different pulse shapes.

The effect of the pulse length is similar to that of an ideal rectangular pulses except for a duration so short that the pulse deviates significantly from the rectangular shape, which happens when the rise and fall times are comparable to the overall pulse length. The corresponding graphs are shown in figure 3.5. The spectrum depicted is for the asymmetric pulse as extracted from circuit simulation, resulting in less distinct spectral nulls at multiples of the data rate.

There are two distinct ways trigger the pulses as shown in figure 3.6: If an ON-level is transmitted over several chips[8], either the oscillator can be turned on once, resulting in a constant envelope throughout the whole sequence, or it can be triggered for every chip. Clearly less energy is conveyed in the second scheme. Thus in the following, only the first one will be considered.

[7]The experiments were conducted by B. Otis.

[8]I use the term *chip* here to refer to one physical pulse, either ON or OFF. This is done to avoid confusion with a *symbol*, which might consist of several chips, depending on the modulation scheme used.

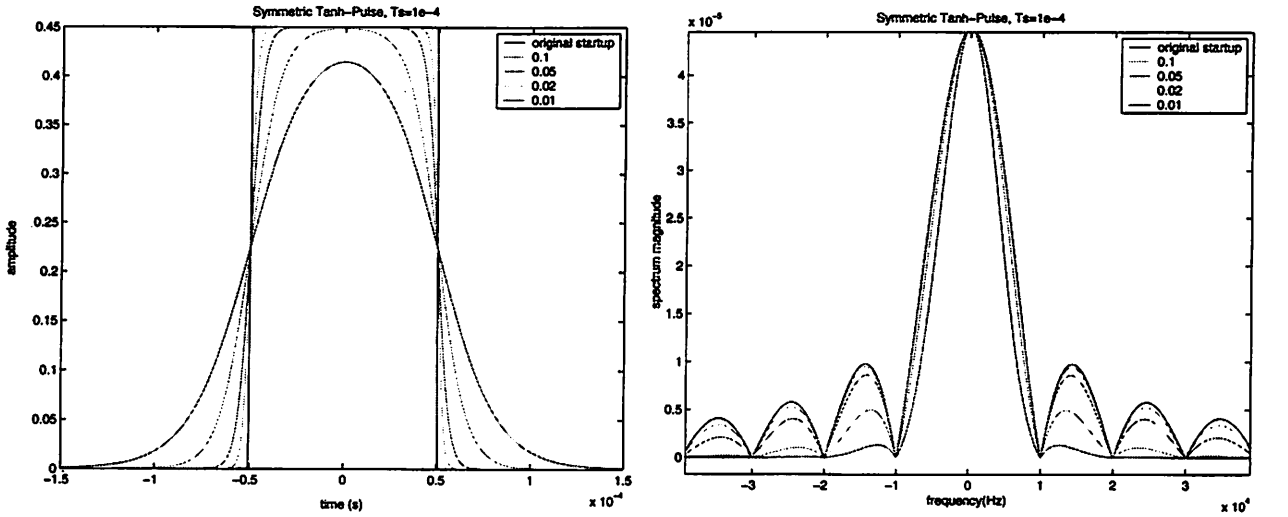

(a) time–domain (b) frequency–domain

Figure 3.4: Pulse Shapes and Spectra for Different Rise–Times

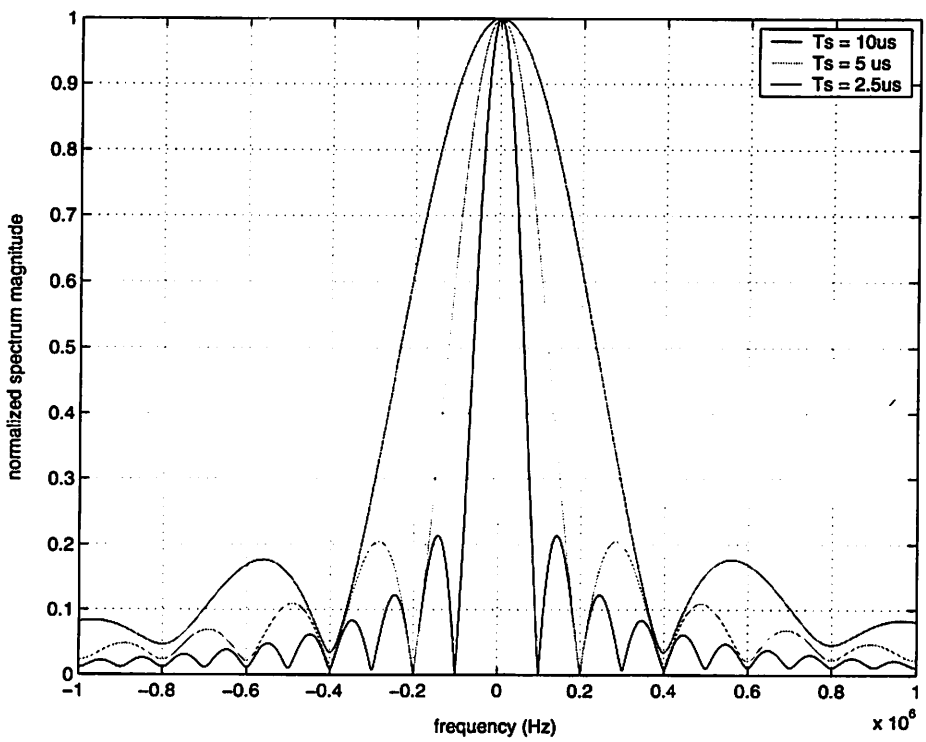

Figure 3.5: Relationship Between Normalized Spectrum and Pulse Width

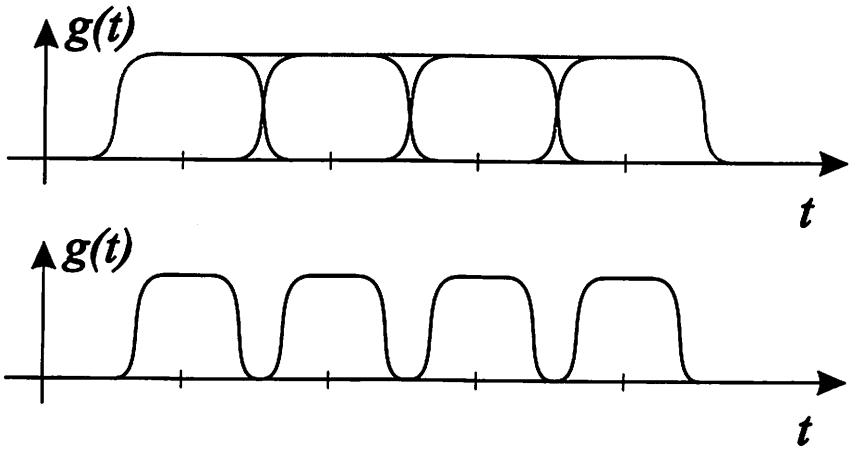

Figure 3.6: Variant of OOK modulation

Following the oscillator and the power amplifier some further filtering will be necessary to suppress the harmonics created by the nonlinear PA. This filter is not included as the simulation bandwidth implicitly acts as a filter.

3.3 Channel

Although the goal of the PicoRadio project is to build a sensor node network consisting of many ubiquitous nodes deployable in many different environments, in the current stage of the project the focus is mainly on indoor office/residential/commercial locations. In the past years, the indoor wireless channel has been thoroughly studied and a variety of models were proposed. A good summary can be found in the book by Rappaport [19] and the survey paper by Hashemi [20]. Models for the indoor channel can be characterized broadly as being *site–specific* or *nonspecific* and *deterministic* or *stochastic*. The nature of the PicoRadio project requires a site–nonspecific model, which is conventionally described by stochastic means. It is common to separate the modeling into large–scale and small–scale effects. Large–scale channel models describe the average path loss as a function of the separation between transmitter and receiver as well as environment parameters (i.e. number of floors, building type, materials, furniture [21] etc.). The large–scale path loss is slowly time varying, hence in the model the path loss is assumed constant. Small–scale models are concerned with the channel behavior over small displacements (on the order of a wavelength) and random fluctuations over time (fading) due to multiple received signals via different paths.

3.3.1 Large–Scale Model

The large scale path loss is caused by the fundamental decay of the received power per unit area with distance and — especially for the indoor environment — due to obstructions in the signal path. The effect of these obstructions, called *shadowing*, is the main contribution to the path loss. Many different channel measurements found a logarithmic dependence on the distance [19]:

$$G_{PL,dB} = G_{PL,0} + 10n\log_{10}\left(\frac{d}{d_0}\right) + X_\sigma \tag{3.6}$$

where the path loss $G_{PL,dB}$ is measured in dB with reference to the path loss $G_{PL,0}$ at some distance d_0 in the far field of the transmitter and n represents the path loss coefficient, a curve–fitting parameter which is obtained from measurements and tabulated for many different sites. X_σ describes the effect of shadowing due to objects in the line of sight (LOS) and modeling uncertainty and is normal distributed in dB with variance σ^2. Additional parameters can be introduced to capture the effect of a transmission across multiple floors and account for different materials of the propagation environment. The path model used here assumes that the nodes will be deployed all on the same floor.

The reference loss in equation (3.6) at the (arbitrary) distance of 1m can be approximated as $G_{PL,0} = -10\log\left(\frac{\lambda^2}{(4\pi)^2 1m}\right) = 38.5dB$ for a carrier frequency of 1.9 GHz and an isotropic antenna with no antenna gain. The path loss model above is only valid for sufficient separation of transmitter and receiver such that the receiver is in the far field. This assumption may be violated as nodes in the PicoRadio system may be placed very close to each other. But with a separation of less than 1m, the received power will be far above the worst–case power considered here.

The maximum range envisioned for the PicoRadio point–to–point link is 10m. With this number and the path loss coefficients summarized by Rappaport from the measurements by Seidel (1992) and Anderson (1994) , the average large–scale propagation loss can be evaluated. The results for different building types are summarized in Table 3.1

A similar model is proposed by the International Telecommunication Union (ITU) [22]

$$G_{PL,dB} = 20\log_{10}\left(\frac{f_c}{1000}\right) + n\log_{10} d + L_f(k) - 28dB \tag{3.7}$$

where $L_f(k)$ is the floor attenuation factor for k floors (or concrete walls). Using the coefficients given in this recommendation, the large–scale path loss is given in Table 3.2 These results

Location	Large–Scale Path Loss in dB	σ in dB
Office 1, soft partition	64.5	14
Office 1, two concrete walls	90.5	14
Office 2	71.2	11.2
Office 3	71	5.2
Grocery Store	56.6	5.2
Retail Store	60.3	8.7

Table 3.1: Large–Scale Path Loss According to Rappaport [19]

Location	Large–Scale Path Loss in dB	σ in dB
Office	67.6	10
Office, two concrete walls	96.6	10
Residential	65.6	8
Commercial	59.6	10

Table 3.2: Large–Scale Path Loss According to the ITU Model [22]

correspond with recent measurements by Patwari et al. [23] (office space, $G_{PL,dB}(10m) = 65$) and Courivaud et al. [24] (engineering lab, $G_{PL,dB}(10m) = 62.8$). The Bluetooth standard also assumes a maximum operating distance of 10m with 0 dBm output power and recommends an average path loss of 62 dB plus a fading margin of 8 dB [6]. Based on these numbers, I chose a slightly pessimistic large–scale path loss of 70 dB as a starting point for the simulations.

3.3.2 Small–Scale Model

The small–scale behavior of the wireless indoor channel depends on the propagation environment, which is generally more diverse than for outdoor channels. The signals traveling over different propagation path combine at the receiver antenna. As different path experience different attenuations and are of different length, constructive or destructive interference occurs, changing the overall received signal strength and phase. Motion of the transmitter, the receiver or the environment (e.g. people walking around) render this process time varying. As a change in path length of the order of a wavelength suffices to substantially change the interference pattern, these fading

effects happen on a faster time scale than changes in the average path loss. The simplest model valid for narrowband RF channels is a time varying linear filter as derived from first principles by Tse [25]. As with the large–scale model, the channel has to be described stochastically if the model should be valid for more than one site.

To characterize the statistical behavior of the channel over time and frequency, the *power delay profile* and the *Doppler power spectrum* are commonly used [26]. To get a more intuitive understanding, two important parameters can be extracted from these functions, permitting a first order approximation of the channel behavior. The *delay spread* is defined as the time range in which paths with significant energy arrive at the receiver. A related measure is the *RMS delay spread*, the second moment of the power delay profile. These delay parameters can be related to the *coherence bandwidth*, over which the channel can be assumed correlated. The second parameter is the *coherence time*, the time period over which the channel stays correlated. Successive symbols will experience approximately the same channel variations as long as they are separated by less than a coherence time. The motion of the transmitter, the receiver and obstacles in the propagation environment directly affect this parameter. For indoor channels, the mobility is generally much lower than for outdoor land–mobile channels, leading to a long coherence time. The number of different path from transmitter to receiver is much larger than in an outdoor environment, but as the propagation distances are in general smaller (especially true for the PicoRadio network with $d < 10m$), the delay spread between the arrival of the first and the last path contributing significant energy can be expected to be smaller as well. From various channel measurements, the characteristic delay parameters are given in Table[9] 3.3.

These numbers were measured under different conditions and are not directly comparable. Most of the channel-measurements are performed for PCS and WLAN applications, where the base stations are normally placed at a higher elevation than the receivers. For the PicoRadio network, receivers and transmitters may be placed arbitrarily, resulting in an atypical delay profile since the ratio of unobstructed to obstructed paths might decrease. To my knowledge, there are no comprehensive measurements for arbitrary transmitter and receiver placements published yet. But this is of no big concern since only the general channel behavior with respect to the transmission bandwidth and the packet length of the PicoRadio system is of interest here. If the extreme cases from the ITU

[9]Both delay spread and RMS delay spread are listed as the sources cited reported their findings in either way.

Source	RMS Delay Spread	Delay Spread
Saleh and Valenzuela (1987) [19] office building	25 ns (median)	100ns (room) 300ns (hallway)
ITU Recommendation P.1238-2 [22] residential office commercial	 20ns — 150ns (rarely) 35ns — 460ns (rarely) 55ns — 500ns (rarely)	
Zepernick and Wysocki (1999) [27] engineering lab	 22ns — 31 ns	 50ns — 67ns
Kurek et al. [28] engineering lab		8.8ns—10.7ns(LOS) 29ns (NLOS)
Kim et al. (1996) [29] engineering lab retail store		 23ns (LOS) — 68ns (NLOS) 35ns (LOS) — 82ns (NLOS)

Table 3.3: Small Scale Delay Parameters from Several Measurements

recommendation are excluded and the RMS delay spread is related to the coherence bandwidth[10] as $B_c = \frac{1}{50\sigma_c}$, the minimum coherence bandwidth is 250 kHz and thus larger than any symbol rate possible with the transmitter described in section 2.1.2. It is therefore a good assumption to model the channel as flat.

Temporal variations are less extensively studied. They are most often assumed to be of considerable duration. Hashemi [20] cites different numbers from various papers, ranging from milliseconds to seconds or even higher, depending on the environment (office space without much motion vs. a crowded shopping center with people moving around constantly). Fades occur over time and may result in a deviation of the path loss from the average value up to 30 dB for the line of sight (LOS) case and 17 dB for the obstructed propagation environment. Temporal variations are roughly captured by the coherence time, which is in turn related to the inverse of the Doppler spread[11]. Measured values for the Doppler spread are normally less than 10 Hz. Assuming that

[10]Here, the coherence bandwidth is defined as the bandwidth for which the correlation function is above 0.9. A relaxed definition would lead to an even larger coherence bandwidth.

[11]The Doppler effect causes the deviation of the received frequency from the transmitted frequency due to relative motion between receiver and transmitter. The Doppler spread is a measure for the range of frequency variation.

the maximum packet length of the PicoRadio system is around thousand bits and the data rate is higher than 10 kbps, it is reasonable to assume that a packet can be transmitted within the coherence time of the channel as the packet duration will be less than 100ms. This result has important implications for the simulation framework in the way the channel effects are simulated: In order to get a good estimate for the bit error rate, the transmission of many (> 100 000) symbols need to be simulated, yet this case never occurs in the actual network as the packets are always much shorter. Thus it makes no sense to include a full–fledged channel, which accurately models the temporal variations. Instead, the bit error rate has to be recorded for different attenuations (according to different fading states of the channel) and then averaged over these states.

3.4 Analog Receiver Front–end

3.4.1 RF Filters

The proposed architecture relies heavily on novel micromachined resonators. The Thin Film Acoustic Bulk Wave Resonator (FBAR) [30] [31] fabricated by Agilent Technologies is a three–layer structure with piezoelectric aluminum nitride in the middle layer. RF signals applied to the electrodes with frequencies near the mechanical resonance frequency excite the bulk compression wave traveling perpendicular to the thin aluminum nitride film. The structure can be used as a standalone second order filter with very high Q ($\approx$ 1000) or in a ladder combination. Both types of filters are used here, the ladder as a broadband receiver front–end filter with high rejection to block out–of–band interferers and the single filter in the oscillator, the power amplifier and the RF amplifier. At present, the FBAR structure is fabricated on a separate die that needs to be bonded to the transmitter and receiver components. The promise of this technology is the possibility of ultimately integrating micromachined filters on the same die as the rest of the transceiver chain. The potential for low power RF applications was demonstrated by Brian Otis [13] with an oscillator consuming an order of magnitude less power than previously published work while showing an excellent phase noise figure.

The FBAR microelectromechanical system is used in different configurations in this system. After a broadband front–end filter consisting of a complex combination of multiple FBAR res-

onators to suppress interferers, a single FBAR is used to provide a more narrowband filtering. In the current front–end design, FBAR filters are incorporated into the tuned RF amplification stage[12] to suppress out–of–band noise. The FBAR is used in lieu of a tuned tank circuit at the drain of the amplifying device, hence the impedance presented by the FBAR determines the filter characteristic.

The magnitude response of a single FBAR filter is plotted in figure 3.7. The very high Q-factor can be observed. For use in the receiver front–end, the carrier frequency is aligned with the parallel resonance, i.e. the high impedance peak. A series resonance at slightly lower frequencies due to the feedthrough path can also be observed. This parallel resonance creates a very sharp dip in the filter response with a rejection of 60 dB. Unfortunately the response is not symmetric around the carrier, with the rejection at frequencies above the carrier significantly less than the rejection at the series resonance. Although the quality factor is very high, the filter is still wide band compared to the signal bandwidth of interest (< 400kHz). This has some important implications for the circuit performance as well as for the simulation framework, as described next.

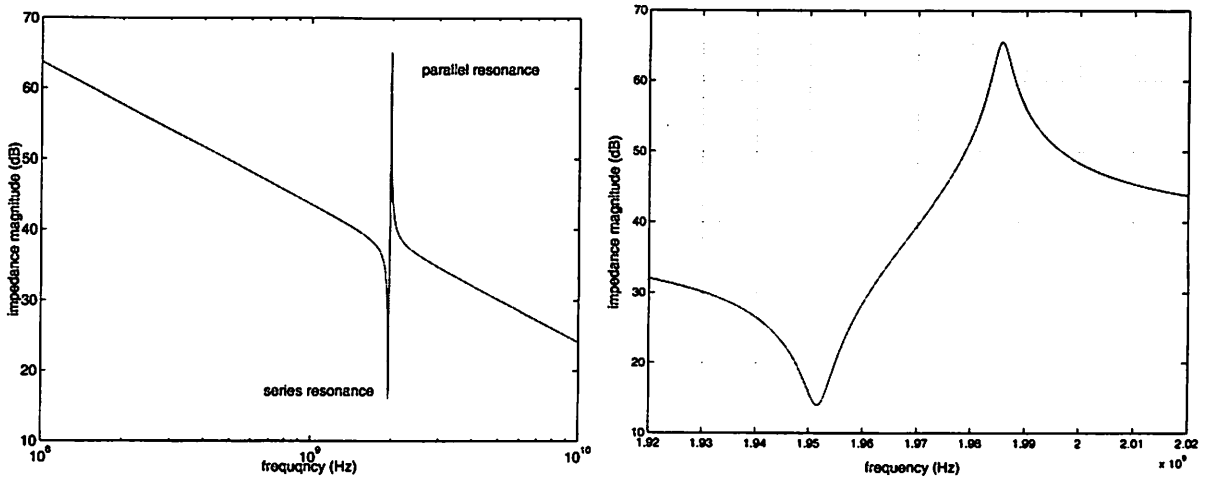

(a) full range (b) zoom around the carrier frequency

Figure 3.7: FBAR Impedance Magnitude

The current system design goal is to provide two independent channels, spaced approximately 30 MHz apart[13] with the passband of the first channel being aligned with the point of maximum rejection of the second channel filter. Due to the non–symmetric frequency response of the FBAR resonators, the second channel cannot be placed at an equivalently convenient location. Both

[12]Designed by R. Lu

[13]This spacing is fixed by the possible resonance frequencies of the FBAR resonators currently available.

channels are located within the passband of the FBAR front–end filter, which is approximately 40 MHz wide. The frequency response shown in figure 3.8 is representative for the one to be used, with a slightly different center frequency. The first channel will be located close to the lower passband edge and the second channel close to the upper one.

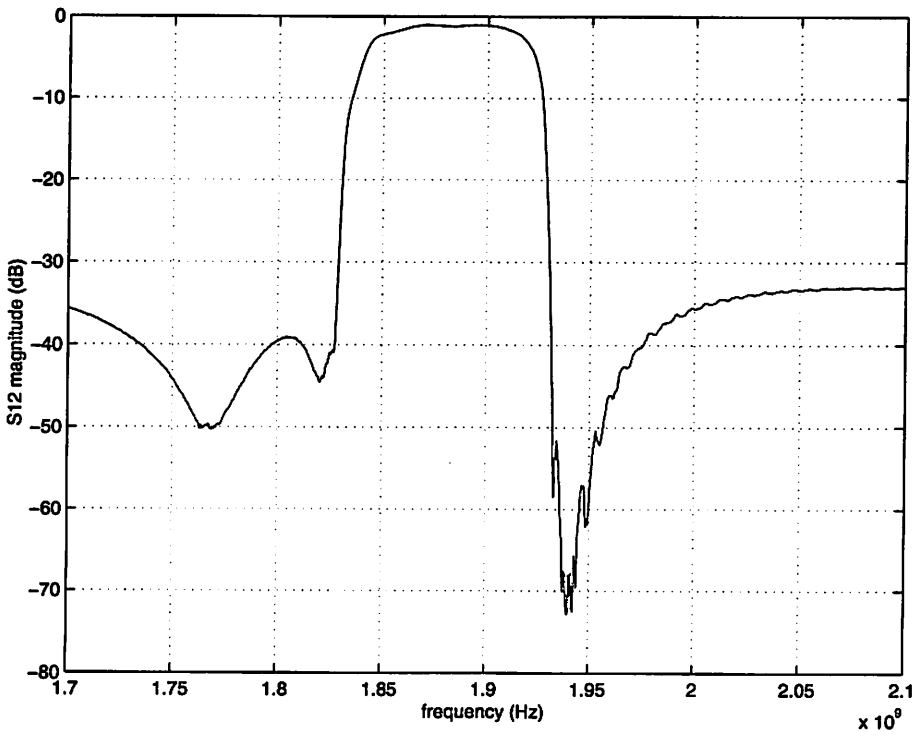

Figure 3.8: FBAR Prefilter Ladder S_{12}

If the channels are to be used simultaneously, the insufficient rejection due to the non–symmetric filter characteristic at frequencies above the carrier will give rise to severe interference problems. Remedies are either improved resonators or an intelligent use of the available channels through coding. These issues are beyond the scope of this work. The focus of the simulation framework is the single–channel point–to–point radio link between two PicoNodes.

3.4.1.1 Simulation Bandwidth Inclusion of interferers at the waveform level is difficult as the interfering signal has to be modeled according to some expected interference pattern. In general the interference performance of narrowband communication systems is very poor and higher–level mechanisms like multiple access protocols have to guarantee correct operation. Hence only the

effect on the received pulse and the noise is included and only the second channel (as defined by the passband in figure 3.7) is modeled. This leads to some modeling difficulty as the carrier frequency, which must be shifted to baseband, is not aligned with the center frequency of the prefilter. However, the effect of the noise passed through the whole frequency range allowed by the front–end is important because the envelope detector described in the next section will introduce a frequency translation, folding the noise spectrum. A reasonable modeling compromise is thus to use a simulation bandwidth of 40 MHz around the carrier frequency of the second channel. With this choice, the model matches the upper edge of the front–end filter on the high side and the strong rejection of the FBAR filter on the low side. The simulation bandwidth acts as an implicit lowpass filter with infinite rejection as all spectral components outside this bandwidth never appear in the simulation. Hence a model for the prefilter does not have to be included. This approach is somewhat optimistic as the rejection of the real system will not be infinite. The insertion loss of the prefilter can be lumped into the path loss of the channel.

3.4.2 Baseband Equivalent Filter Models

For modeling purposes, I separate the two functions, amplification and filtering with the filter following the amplifier. The goal is thus to derive a baseband equivalent model of the FBAR impedance transfer function in the frequency range of interest, capturing the important aspects of its response. In general for a baseband equivalent model to exist, the bandpass system has to be band–limited. This is evidently not the case for the FBAR response. A capacitive feedthrough path exists between the plates of the resonator, resulting in a pole at the origin.

The FBAR can be described via an equivalent electric circuit model, called the lumped Butterworth–Van–Dyke model. Larson et al. proposed a modified version, including a resistance in series with the plate capacitance to model parasitic losses [32]. The corresponding circuit is shown in figure 3.9. C_0 models the plate capacitance, R_0 is the modeling resistance and C_m, R_m and L_m represent the motional resonance. The terminal impedance is thus given by

- resonator path

$$Z_x(s) = \frac{1}{sC_x} + sL_x + R_x \tag{3.8}$$

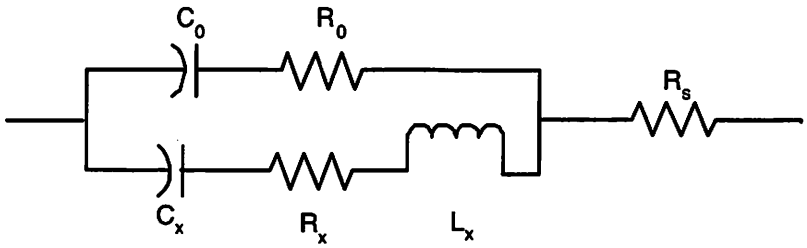

Figure 3.9: FBAR Equivalent Electric Circuit Model

- feedthrough path

$$Z_0(s) = \frac{1}{sC_0} + R_0 \tag{3.9}$$

Hence the overall impedance is

$$Z(s) = \frac{\left(R_0 + \frac{1}{C_0 s}\right)\left(R_x + \frac{1}{C_x s} + L_x s\right)}{R_0 + R_x + \frac{1}{C_0 s} + \frac{1}{C_x s} + L_x s} \tag{3.10}$$

where the values for the modeling components are $R_x = 1.7\Omega$, $L_x = 190nH$, $C_x = 35fF$, $R_0 = 1.7\Omega$ and $C_0 = 1pF$.

The first step in deriving a baseband equivalent model is to gain some insight into the transfer characteristic by expanding (3.10) into partial fractions:

$$Z(s) = R_0 + \frac{1}{(C_0 + C_x)\, s} + \frac{-2C_0C_xR_0 - C_x^2(R_0 + R_x) + [C_x^2L_x - C_0^2C_xR_0^2 - C_0C_x^2R_0^2]\, s}{(C_0 + C_x)\,[C_0 + C_x + C_0C_x\,(R_0 + R_x)\, s + C_0C_xL_xs^2]} \tag{3.11}$$

For convenience, I define

$$\begin{aligned} Z_1(s) &= \frac{1}{(C_0 + C_x)\, s} \\ Z_2(s) &= \frac{-2C_0C_xR_0 - C_x^2(R_0 + R_x) + [C_x^2L_x - C_0^2C_xR_0^2 - C_0C_x^2R_0^2]\, s}{(C_0 + C_x)\,[C_0 + C_x + C_0C_x\,(R_0 + R_x)\, s + C_0C_xL_xs^2]} \end{aligned} \tag{3.12}$$

A comparison of the magnitude response of the FBAR system and the second order system $Z_2(s)$ is shown in figure 3.10. This approximation holds reasonably well (1 dB difference) within 5 MHz of the carrier and degrades for higher bandwidth. The advantage of using only $Z_2(s)$ to approximate the FBAR characteristic is a very simple implementation of the baseband equivalent model. This single pole system can be approximated in discrete time via the bilinear transform as described by Oppenheim [33]. A baseband simulation bandwidth of 5 MHz though is not appropriate because

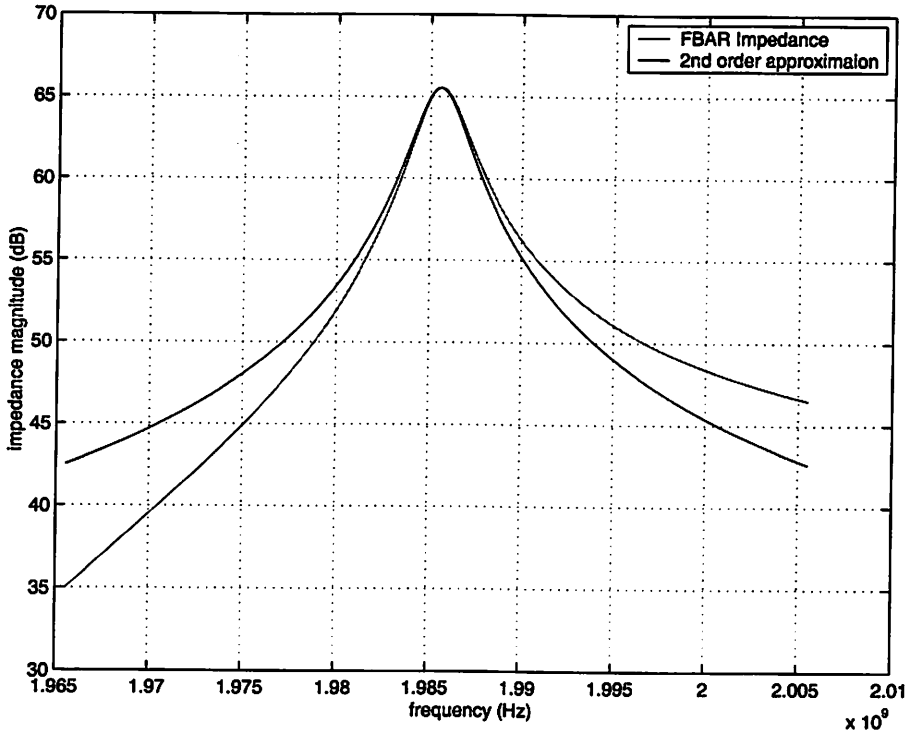

Figure 3.10: Comparison of FBAR Impedance and $Z_2(s)$

as discussed above, the effect of wideband noise not sufficiently attenuated by the filter might have a significant impact on the system.

The second order system $Z_2(s)$ can be analyzed in a convenient way using the Laplace Transform[14] pair

$$\frac{b(s+\alpha)}{(s+a)^2+\omega_0^2} \longleftrightarrow \frac{b}{\omega_0}\sqrt{(\alpha-a)^2+\omega_0^2}e^{-at}\sin(\omega_0 t+\phi) \qquad \text{where} \quad \phi = \arctan\frac{\omega_0}{\alpha-a} \tag{3.13}$$

where ω_0 is the resonance frequency of the second order system. After some algebraic manipula-

[14]Throughout the text I use the single sided Laplace transform given by

$$F(s) = \int_0^\infty f(t)e^{st}\mathrm{dt}$$

tion, the parameters can be identified as

$$\begin{aligned} a &= \frac{R_0 + R_x}{2L_x} \\ \alpha &= \frac{2C_0R_0 + C_xR_0 - C_xR_x}{-C_xL_x + C_0^2R_0^2 + C_0C_xR_0^2} \\ b &= \frac{C_xL_x - C_0^2R_0^2 - C_0C_xR_0^2}{C_0^2L_x + C_0C_xL_x} \\ \omega_0 &= \sqrt{\frac{C_0 + C_x}{C_0C_xL_x}} - \frac{R_0 + R_x}{2L_x} \end{aligned} \tag{3.14}$$

With the use of trigonometric identities, the impulse response in equation (3.13) can be expressed as the sum of two modulated envelopes:

$$h_2(t) = \frac{b}{\omega_0}\sqrt{(\alpha - a)^2 + \omega_0^2}e^{-at}\left[\sin(\phi)\cos(\omega_0 t) + \cos(\phi)\sin(\omega_0 t)\right] \tag{3.15}$$

Hence the complex baseband equivalent envelope is

$$h_{2b}(t) = \frac{b}{\omega_0}\sqrt{(\alpha - a)^2 + \omega_0^2}e^{-at}\left[sin(\phi) + jcos(\phi)\right] \tag{3.16}$$

This is just the impulse response of a first order lowpass filter with the pole given by a. The 3dB bandwidth is thus 1.42 MHz. The overall simulation bandwidth has to be at least 5 times higher than this 3dB–bandwidth in order for the pseudo–random number generator to produce an approximately white noise process [4]. This constraint is satisfied by the chosen simulation bandwidth of 40 MHz.

To obtain a better model, the effects of the second term ($Z_1(s)$) in equation (3.10) have to be included. But the additional term cannot accurately be approximately as bandlimited around the carrier. $Z_2(s)$ was already in the amenable form of a modulated envelope whereas the time-domain equivalent of an ideal integrator like $Z_1(s)$ is the unit step function. Since the bandwidth W of the simulation is limited to half the chosen sampling frequency, a valid approach is to first limit the bandwidth of the system under consideration to W around the carrier frequency, thus circumventing problems arising from the asymptotic behavior for $f \rightarrow 0$, and then to shift the filtered part to baseband. The resulting system must be sampled and truncated to obtain a discrete–time impulse response suitable for simulation. Because the derivation of this impulse response is not very insightful, it is moved to the appendix. To obtain a reasonably close approximation, the sampled impulse response must capture a large part of the energy contained in the original response. Since the decay is dominated by the *sinc*–term due to the bandlimiting operation, the impulse response

decays only as $\frac{1}{t}$, necessitating a filter with many taps. A better way is to use frequency domain filtering techniques based on the Discrete Fourier Transform. Because the filter response is specified in the frequency domain already, this provides the additional benefit of avoiding cumbersome manipulations of the impulse response.

Frequency domain filtering relies on the convolution theorem of the DFT. The periodic convolution of two discrete time sequences is equivalent to the multiplication of their DFTs. To use this fact for non–periodic sequences[15] they have to be zero–padded up to the length of the resulting convolution which is $M + N - 1$, where M and N are the lengths of the sequences. These sequences are then transformed using efficient FFT algorithms, multiplied, and transformed back to the time–domain. Jeruchim [17] shows that this scheme needs $N_1 = L \log_2 L + L$ multiplications compared to $N_2 = (M + N) L$ multiplications for the equivalent time domain convolution. Here L is the maximum length of the two sequences M and N. The incoming signal is in general a very long stream so it has to be broken up into shorter sequences of length N.
Since the goal is to operate directly on the frequency domain filter response, I have to take into account the zero–padding performed in the time domain. If the FFT-length is $K = M + N - 1$, K frequency domain points are needed for the filter response; but these K point cannot be obtained by just sampling the frequency response, as this would yield an impulse response of likewise K points, violating the constraint on the sequence length to avoid aliasing in the time domain due to the periodic convolution property. The correct procedure is to obtain M frequency domain points, shift them to their equivalent baseband location, take the inverse Fourier transform, pad the sequence with zeros to obtain a sequence of length K and compute the frequency response of this new sequence using the DFT. For M frequency samples, the effective frequency response is obtained by interpolation with a *sinc* function:

$$Z_M(f) = \sum_{l=-\frac{M}{2}}^{\frac{M}{2}-1} Z\left(j2\pi(lF + F_0)\right) \operatorname{sinc}\left(\frac{f - F_0 - lF}{F}\right) \tag{3.17}$$

with F_0 the center frequency and F the frequency spacing $F = \frac{W}{k}$. The result of this approach is shown in figure 3.11 for 80 samples in the bandwidth of interest. Notice the error at the band edges. This is due to the Gibbs phenomenon and cannot be resolved by using more sampling points. Windowing can mitigate this effect, but is unnecessary in this model as the frequency response at

[15]This is a standard algorithm which is described in many textbooks [33], [34], so I refrain from presenting it in detail here.

the band edges is already inaccurate due to the compromise between simulation bandwidth and prefilter characteristic described earlier.

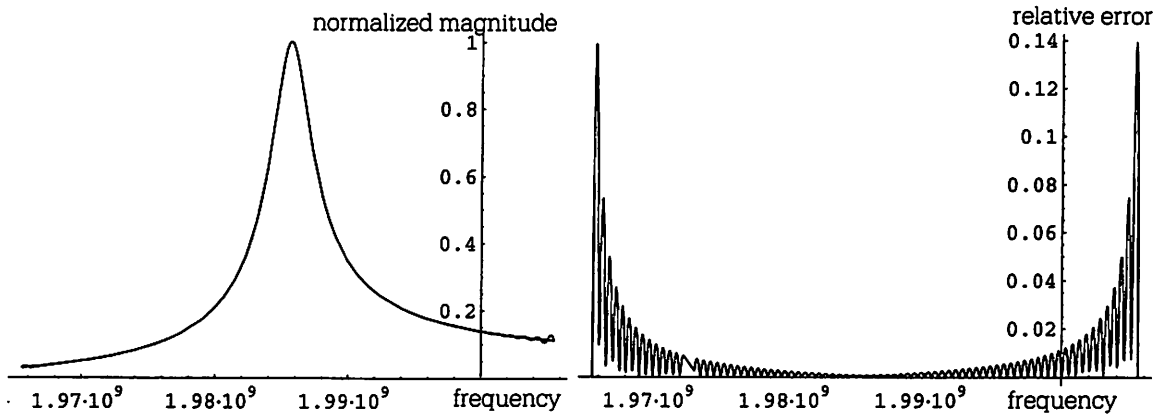

(a) Frequency Response and Interpolation (b) Relative Error

Figure 3.11: Frequency Response Interpolation, 80 Samples

3.5 Envelope Detector

3.5.1 Ideal Noncoherent Detection

One of the core components of the proposed receiver architecture is the envelope detector. In early AM radio receivers, an envelope detector was the preferred way of extracting the modulated audio signal from the carrier as the implementation was cheap and the performance sufficient for the analog radios of these days. In digital communication systems, envelope detectors are used for incoherent reception of the transmitted signal, i.e. the phase information is discarded. This facilitates the design of the synchronization unit at the cost of a lower signal to noise ratio. In fact, for a fading channel, incoherent reception is the only possibility if the channel is not estimated at the receiver. However, in the typical radio architecture of a digital communication system employing noncoherent demodulation, the envelope detector is only used to average over the unknown receiver phase, the signal is still demodulated by a mixer and subsequently filtered by a matched filter [34], [26] as the envelope detection before matched filtering alters the statistics of the noise [35]. To illustrate this point, consider a bandpass signal $g(t)\cos(2\pi f_c t)$ with carrier frequency f_c, where $g(t)$ is a baseband waveform. In the special case of a rectangular pulse with

amplitude A, two separate cases can be identified, *signal present* and *signal absent.* The signal is corrupted by band-limited additive white Gaussian noise, where the quadrature terms $n_I(t)$ and $n_Q(t)$ are independent with equal variance $Var\left(n_I(t)\right) = Var\left(n_Q(t)\right) = \sigma_n^2$:

$$s(t) = (A + n_I(t))\cos(2\pi f_c t) - n_Q(t)\sin(2\pi f_c t) \tag{3.18}$$

Transforming the bandpass process $s(t)$ into a polar representation with the envelope $env(t) = \sqrt{x_I^2(t) + x_Q^2(t)}$, the marginal probability density function of the envelope is [26]:

$$p_{env}(r) = \frac{r}{\sigma_n^2}\exp\left(\frac{-r^2 - A^2}{2\sigma_n^2}\right) I_0\left(\frac{Ar}{\sigma_n^2}\right) \tag{3.19}$$

This is the *Rician* pdf with the modified Bessel function of the first kind and order zero I_0. As the noise after envelope detection, i.e. performing the operation $\sqrt{x_I^2(t) + x_Q^2(t)}$ is no longer Gaussian, the classical optimal receiver consisting of a matched filter, sampler and slicer is no longer the optimal maximum likelihood detector.

3.5.2 The Envelope Detector as a Demodulator

The envelope detector in the PicoRadio architecture not only serves to remove the phase dependency but to perform the complete downconversion operation. In principle any memoryless nonlinearity followed by a lowpass filter is suited for this task. Expanding the transfer function of the nonlinearity into a power series of the form $y(t) = a_0 + a_1 x(t) + a_2 x(t)^2 + \ldots$, and using the trigonometric theorems $\sin^2(2\pi f_c t) = \frac{1}{2}\left[1 - \cos(4\pi f_c t)\right]$ and $\cos^2(x) = \frac{1}{2}\left[1 + \cos(4\pi f_c t)\right]$, it is apparent that a frequency translation has taken place, yielding a term at baseband and one at double the carrier frequency. Yet it is important to realize that the envelope detector is located before the matched filter in the receiver chain, introducing a nonlinear transformation of the received pulse and the noise. As already mentioned, this nonlinear transformation of the noise alters its statistics. Let's take a closer look at these effects. Assume the nonlinearity is sufficiently approximated by a third order power series. To facilitate calculations I assume further that the nonlinearity does not have a dc-term (i.e. a_0 is zero). Using the bandpass representation (3.18) with some pulse shape $g(t)$ instead of the constant amplitude A, I obtain after some algebraic manipulations

$$\begin{aligned} v(t) &= \frac{1}{2}\left[g(t) + n_I(t)\right]^2 + \frac{1}{2}n_Q(t)^2 \\ &= \frac{1}{2}g(t)^2 + g(t)n_I(t) + \frac{1}{2}n_I(t)^2 + \frac{1}{2}n_Q(t)^2 \end{aligned} \tag{3.20}$$

Thus at every epoch t, the process $v(t)$ has a *chi-square* distribution, which is consistent with the Rician distribution derived earlier, as the square-root operation on the output signal is omitted. The important aspects here are waveform distortion since the squaring of the transmitted leads to an increase in bandwidth[16], squaring of the noise, and modulation of the noise by the signal.

A sampled matched filter after the envelope detector is no longer the optimal detector, but it is easily implemented and of low complexity. Assume again ideal rectangular pulses[17] and investigate the heuristic approach of integrating over a signal interval T in order to maximize the received signal energy. Integration of (3.20) yields

$$V = \frac{1}{2}\int_0^T g(t)^2 \mathrm{d}t + \int_0^T g(t) n_I(t) \mathrm{d}t + \frac{1}{2}\int_0^T \left(n_I(t)^2 + n_Q(t)^2\right) \mathrm{d}t \tag{3.21}$$

The first two terms in (3.21) are exactly the same as obtained for a linear receiver with a correlator type detector. The last term is the integration of the band–limited noise envelope, which is chi-square distributed at each epoch. Assuming that the central limit theorem holds, the last term is also approximately Gaussian, but not zero mean. For an ergodic noise process, the time average approaches the ensemble average and thus this term can be interpreted as contributing additional noise power. The effect of the nonlinearity for this particular detection scheme hence yields a degradation in SNR proportional to the power of the integrated squared noise.

3.5.3 Envelope Detector Implementation

The discussion thus far was only concerned with idealized models of the nonlinearity, in particular the memoryless power series representation. Designing a circuit with this transfer function is difficult in MOS technologies. The realization of translinear function circuits in bipolar technologies depending on the exponential BJT transfer characteristic is easier. But subthreshold MOS devices also approximate the exponential transfer characteristic, a fact which is exploited in the envelope detector investigated here (figure 3.12)[18]. The design follows the circuit described by Meyer [36], with MOSFET devices operating in the subthreshold region instead of bipolar transistors.

[16] A squaring operation in the time domain is equivalent to a convolution of the pulse spectrum with itself in the frequency domain, hence for bandlimited (physical) pulses, the bandwidth will always increase.

[17] Which is quite a good approximation for the pulses as already seen.

[18] The envelope detector was designed and implemented by Brian Otis for the first PicoRadio RF test chip.

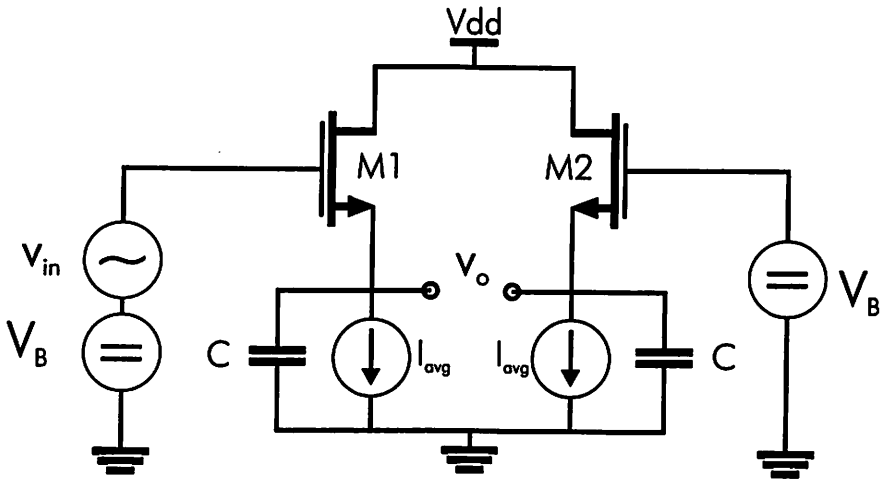

Figure 3.12: Envelope Detector Schematic (simplified)

3.5.4 Behavioral Model

A suitable model for implementation in a system level simulation framework should capture the important behavioral aspects of the building block while being as simple as possible to increase simulation speed. Compared with a full-fledged circuit level simulation, where devices are modeled with high accuracy in all operation regions, this model only has to hold for the operation in the typical region over a sufficient range of the input signal.

3.5.4.1 Models for Nonlinear Circuits To model the behavior of a nonlinear system, various approaches can be followed [17]. They differ mainly in the complexity of the equations describing the transient behavior of the nonlinear elements. The power-series approach already used earlier is easy to use, yields fast simulation times and is fairly accurate for a big class of systems. The coefficients of the power series can be obtained via harmonic distortion measurements (HD_2, HD_3) or, if measurements are not readily available, via distortion simulations like SPECTRE'S Periodic Steady State (PSS) analysis. For circuits exhibiting a highly nonlinear behavior, the power-series approach may result in a high-order polynomial to achieve the desired accuracy. If it is possible to obtain an analytical expression of the steady state transfer function of the circuit, it may be used instead of a power series. This approach is used for the envelope detector and is described below.

The power series approach is only suitable for *memoryless* nonlinearities. However, in many

cases, the system can be separated into a linear filter and a memoryless nonlinearity. For more involved systems, a generalization of the power-series approach, the *Volterra-Series*, can be used to model a frequency-dependent nonlinearity [37]. The system identification, i.e. the process of obtaining the Volterra Kernels from measurements or circuit simulations, is involved. Fortunately, the envelope detector can be sufficiently modeled as a memoryless nonlinearity followed by a linear filter, as will be described now.

3.5.4.2 CMOS Envelope Detector Transfer Characteristic The envelope detector used is derived from the one described by Meyer [36], implemented in a bipolar technology. To model the behavior, I follow Meyer's approach deriving a transfer function starting from the device equations. The signal modulated onto a carrier gets transformed by the exponential device characteristic. Expanding this transfer characteristic into a Fourier Series, the baseband signal component can be obtained and the result further simplified by means of a Taylor expansion, leading to the description of the nonlinear behavior in terms of a power series.

First consider an input signal of the form $v(t) = g(t)\cos(2\pi f_c t)$ and neglect any noise terms. The envelope $g(t)$ varies slowly compared to the carrier of frequency f_c. Assume further that the capacitor C is large enough so that the output voltage drop during one cycle of the input sinusoid is negligible. Let the voltage at the source of M_1 be denoted $V_a(t)$ and the bias voltage at the gate V_B. The devices are biased to operate in weak inversion, thus the drain current is determined by the operation of the parasitic lateral bipolar transistor with the following transfer characteristic [38]:

$$I_D = \frac{W}{L} I_t \exp\left(\frac{V_{GS}}{nV_T}\right) \exp\left(\left[1 - \frac{1}{n}\right]\frac{V_{BS}}{V_T}\right) \tag{3.22}$$

where n is a process dependent constant between 1 and 2, caused by the imperfect control of the base region of the parasitic BJT through the capacitive divider between the gate capacitance and the depletion layer capacitance[19].

The gate-to-source voltage V_{GS} is the difference between the sum of the fixed bias voltage V_B and the time-varying input $v(t)$ at the gate, and the source voltage $V_a(t)$. Note that strictly speaking this is inconsistent with the assumptions of a constant source voltage, as $V_a(t)$ is time varying. The key here is to recognize that there are two different time scales separated by several orders of

[19] In a dedicated bipolar transistor, the base depletion region width is directly modulated by the base-emitter voltage.

magnitude: the *carrier timescale* defined by the carrier frequency on the order of $2GHz$ and the *symbol timescale* on the order of tens of kHz[20]. The voltage at the source is only varying with the envelope of the input signal and is thus approximately constant over a period of the carrier. It is thus possible to write

$$\begin{aligned} I_{d1}(t) &= I_{S1} e^{\frac{V_B - V_a(t)}{nV_T}} e^{-\frac{n-1}{nV_T} V_a(t)} e^{\frac{v(t)}{nV_T}} \\ &= I_{S1} e^{\frac{V_B}{nV_T}} e^{\frac{V_a(t) - (n-1)V_a(t)}{nV_T}} e^{\frac{v(t)}{nV_T}} \\ &= I_{S1} e^{\frac{V_B}{nV_T}} e^{-\frac{V_a(t)}{V_T}} e^{\frac{v(t)}{nV_T}} \end{aligned} \tag{3.23}$$

The exponential term depending on the input signal can be expanded into a Fourier Series, once again assuming that the envelope is approximately constant on the carrier timescale. For a constant b [39]

$$e^{b\cos(2\pi f_c t)} = I_0(b) + 2I_1(b)\cos(2\pi f_c t) + 2I_2(b)\cos(4\pi f_c t) + 2I_3(b)\cos(6\pi f_c t) + \ldots \tag{3.24}$$

where the $I_n(b)$ are modified Bessel functions of the first kind and order n. The derivation of this series expansion as well as the one for $e^{b\sin(2\pi f_c t)}$ needed later on is postponed to appendix B. I may now substitute the signal envelope $g(t)$ for the constant b.

The average value of (3.23) is obtained by the low-pass filter consisting of C and the finite source resistance of the current source I_1 and - if needed - further filtering in subsequent stages. But this average drain current is equal to I_1. Hence

$$I_1(t) = I_{S1} e^{\frac{V_B}{nV_T}} e^{-\frac{V_a(t)}{V_T}} I_0\left(\frac{g(t)}{nV_T}\right) \tag{3.25}$$

The second branch of the envelope detector, set up to provide a fixed reference voltage, is designed to carry equal steady state current while maintaining the same source voltage as the active left branch in steady state. Assuming perfectly matched devices, the currents are equal: $I_{S1} = I_{S2}$ and $I_1 = I_2 = I_{avg}$. Let V_A denote the fixed source voltage of the right branch. Hence

$$I_2 = I_{S2} e^{\frac{V_B}{nV_T}} e^{-\frac{V_A}{V_T}} \tag{3.26}$$

[20]Unfortunately this separation is still not sufficient for further derivations as the bandwidth of the baseband envelope $g(t)$ is of importance. Assuming perfectly rectangular pulses, the bandwidth clearly is not finite. But this is merely a modeling artifact and not a physical reality, thus I will continue to use the rectangular approximation for mathematical convenience, keeping in mind that the physical system is bandlimited to a bandwidth orders of magnitude smaller than the carrier frequency.

Equating the currents yields

$$I_{S1}e^{\frac{V_B}{nV_T}}e^{-\frac{V_a(t)}{V_T}}I_0\left(\frac{g(t)}{nV_T}\right) = I_{S2}e^{\frac{V_B}{nV_T}}e^{-\frac{V_A}{V_T}} \tag{3.27}$$

$$\Rightarrow e^{-\frac{V_a(t)}{V_T}}I_0\left(\frac{g(t)}{nV_T}\right) = e^{-\frac{V_A}{V_T}} \tag{3.28}$$

The differential output voltage is defined as the difference between the two source voltages $V_o(t) = V_B - V_A - V_B + V_a(t) = V_a(t) - V_A$, hence

$$V_o(t) = V_T \ln\left(I_0\left(\frac{g(t)}{nV_T}\right)\right) \tag{3.29}$$

This equation describes the voltage transfer characteristic of the nonlinear part of the envelope detector. Note that it relates the input envelope to the output signal and is thus a baseband equivalent transfer characteristic. The subthreshold degradation coefficient n can be set in order to obtain good matching between the analytical model and measurements or circuit simulations. In this case, $n = 1.3$ yields a very close match in the region of interest as compared to circuit simulations. As can be seen in figure 3.13, the matching is quite good for steady–state inputs, where sinusoids of different amplitudes are applied to the circuit. Note that the gain of the detector is less then one and the curve flattens out for very low input voltages. This will cause problems in overcoming the noise of the detector devices, as discussed later on.

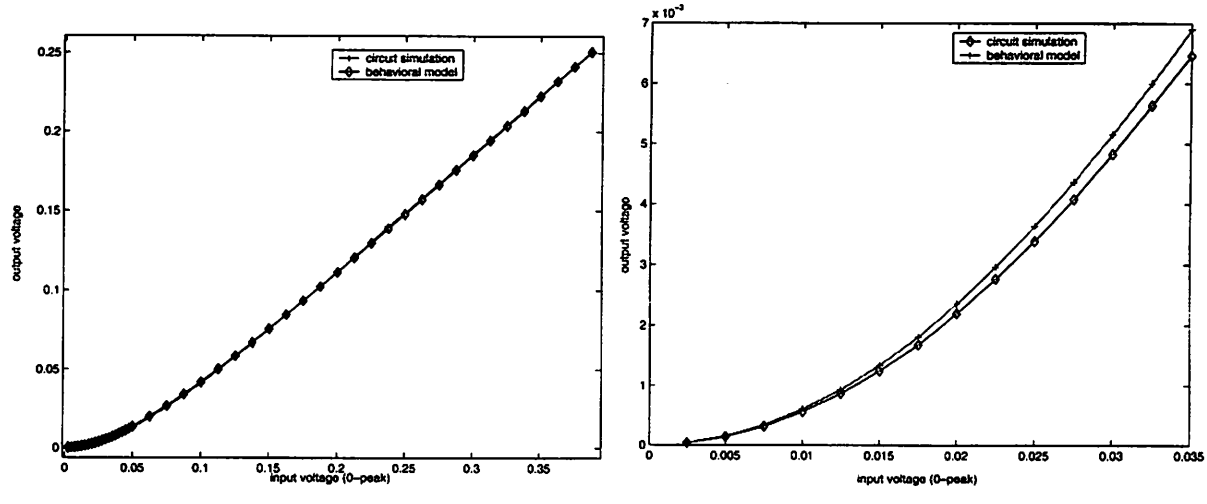

(a) full range

(b) zoom for low input voltages

Figure 3.13: Envelope Detector Steady State Transfer Characteristic

For time varying signals, the lowpass filtering has to be included. The detector is designed for a fundamental time constant of $\tau = 333nS$ to allow for a settling time of approximately $1\mu s$.

Therefore the first order lowpass filter due to C has a cutoff frequency of 480kHz. Comparisons between circuit simulations and the cascade of the nonlinear transfer function (3.29) and a first order lowpass filter deviate from this number and show very good matching for a first order lowpass filter with a bandwidth of 400kHz. This difference can be attributed to the additional parasitic capacitances not taken into account in the behavioral model, as the power series approach implicitly neglects the effects of all circuit elements with memory. Transient simulation results are shown in the following plots. For input voltages in the range between $10mV$ and $40mV$, the results again match the analytical curve very well. For higher input voltages, an increasing steady state error can be observed. but this error is not a big concern here, as the radio performance is limited by the operation region resulting in the minimal detectable signal, which is around $10mV$.

A further approximation of the transfer characteristic can be obtained by expanding (3.29) into a Taylor Series around the small signal equilibrium, yielding

$$V_o(t) = V_T \left(\frac{1}{4} \left(\frac{g(t)}{nV_T} \right)^2 - \frac{1}{64} \left(\frac{g(t)}{nV_T} \right)^4 + \frac{1}{576} \left(\frac{g(t)}{nV_T} \right)^6 + o\left[\left(\frac{g(t)}{nV_T} \right)^8 \right] \right) \tag{3.30}$$

This illustrates that the nonlinearity is mainly quadratic. As expected, no odd-order terms are present in the baseband envelope transfer function.

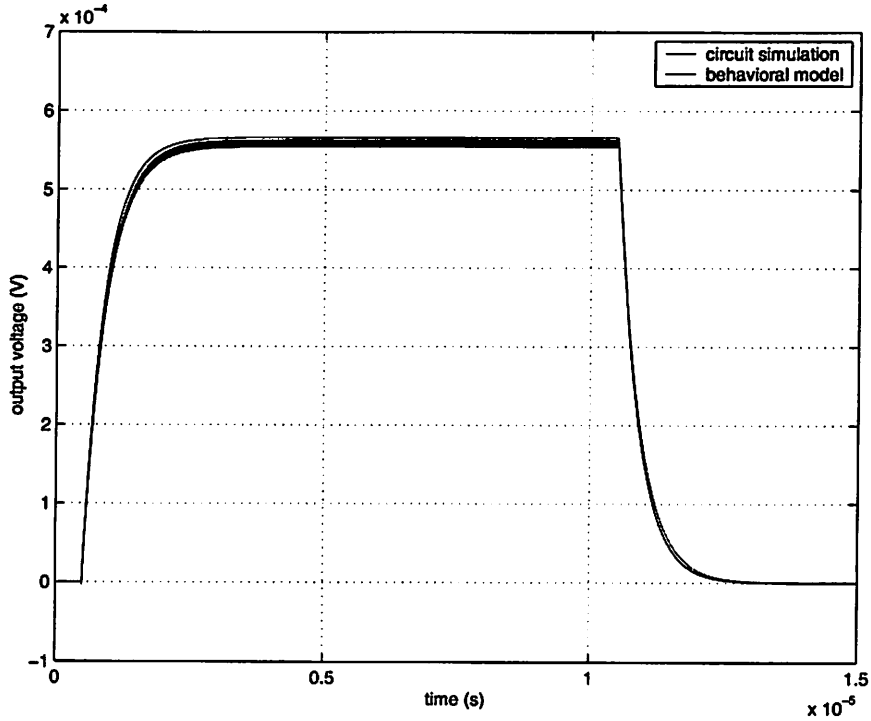

(a) 10mV Amplitude

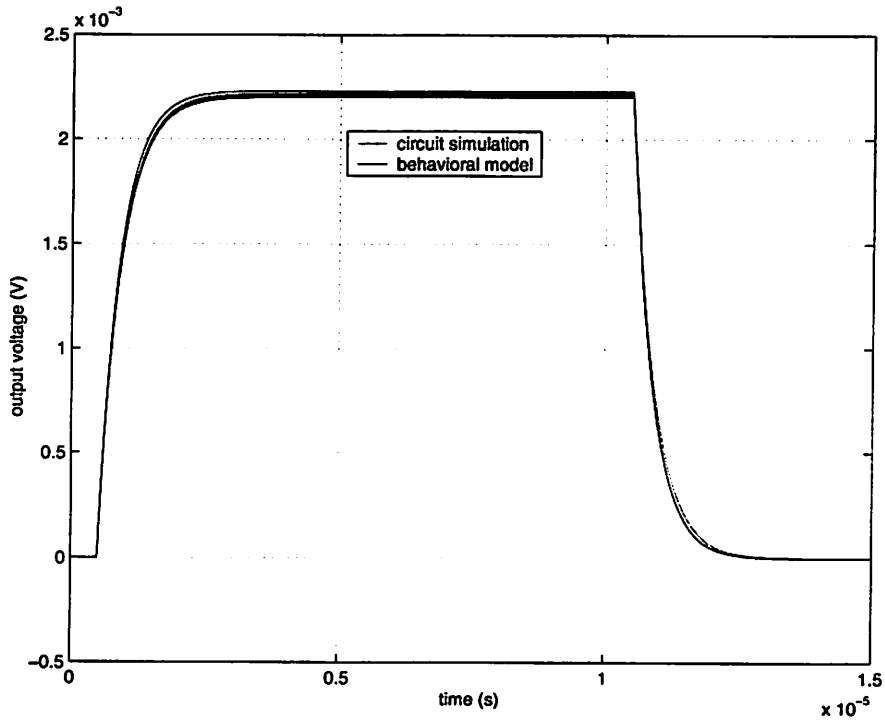

(b) 20mV Amplitude

Figure 3.14: Transient Transfer Characteristic for an Ideal Rectangular Pulse with 10mV and 20 mV Amplitude respectively

3.5.4.3 Measurement Results The envelope detector was implemented in STMicroelectronic's $0.13\mu m$ process. The measured curves deviate from the ones predicted by the model quite signifi-

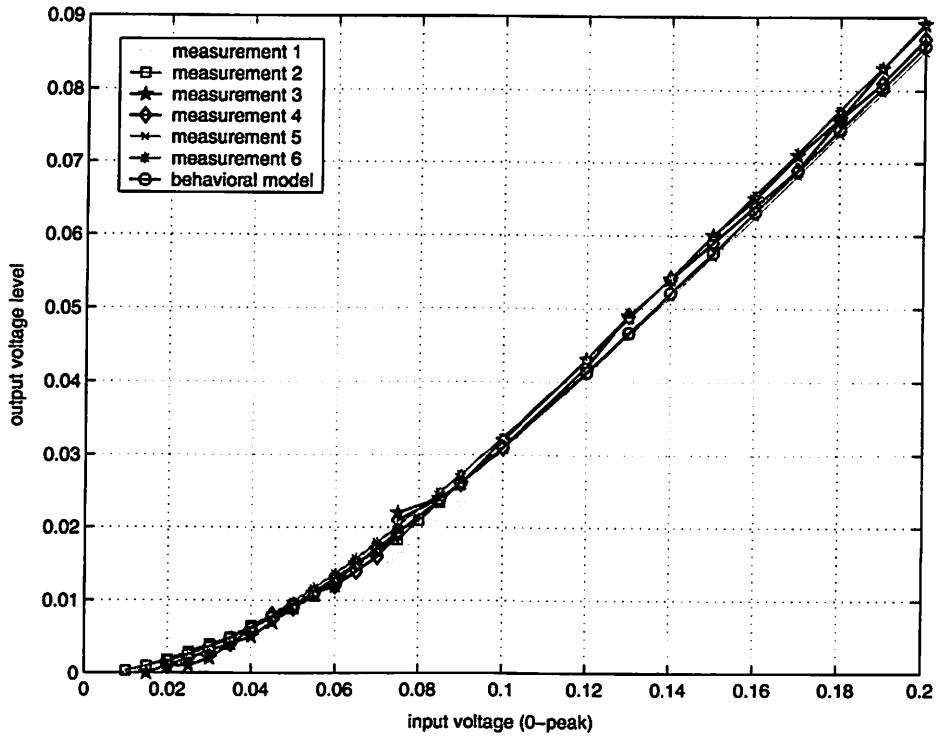

Figure 3.15: Measured Stationary Envelope Detector Transfer Characteristic

cantly. This difference can be attributed to incorrect device models, as for a different subthreshold coefficient n, a very good matching can be achieved once again. The curve predicted by the behavioral model is also plotted figure 3.15, along with measurements taken across three different dies. This time a subthreshold coefficient of $n = 1.54$ is used. A critical metric is the useful range of the detector, which by observation is limited on the lower end at around $15mV$. This limitation is due to of the noise floor. the measurement setup always contributes additional noise, but as will be discussed in section 3.6,the noise of the detector itself may limit the useful range of the circuit.

3.5.4.4 Extended Transfer Characteristic Thus far I only examined a signal with a real envelope modulated by a cosine carrier. Although the system described here does not employ quadrature modulation, the unknown phase induced by the channel and the noise may change the envelope detector response (3.29). A general bandlimited passband signal is of the form

$$r(t) = g_I(t)\cos(2\pi f_c t) - g_Q(t)\sin(2\pi f_c t) \tag{3.31}$$

where $g_I(t)$ and $g_Q(t)$ are the inphase and quadrature components respectively, including signal and additive noise terms.

Starting from equation (3.23) and replacing the input signal $v(t)$ by (3.31), the general formulation for the drain current in M1 is

$$I_1(t) = I_{S1} e^{\frac{V_B}{nV_T}} e^{-\frac{V_a(t)}{nV_T}} e^{\frac{1}{nV_T}\left(g_I(t)\cos(2\pi f_c t) - g_Q(t)\sin(2\pi f_c t)\right)} \tag{3.32}$$

As before, the exponential terms depending on the carrier frequency can be expanded into a Fourier–Series. To simplify notation, define $b_c := \frac{g_I(t)}{nV_T}$ and $b_s := \frac{g_Q(t)}{nV_T}$. Using the expansions derived in the appendix , I may write

$$s(t) := e^{b_c \cos(2\pi f_c t)} e^{-b_s \sin(2\pi f_c t)} = \left[I_0(b_c) + \sum_{n=1}^{\infty} 2I_n(b_c)\cos(2n\pi f_c t) \right] \tag{3.33}$$
$$\times \left[I_0(-b_s) + 2I_1(-b_s)\sin(2\pi f_c t) - 2I_2(-b_s)\cos(4\pi f_c t) - 2I_3(-b_s)\sin(6\pi f_c t) + \ldots \right]$$

The lowpass–characteristic of the envelope detector rejects all terms modulated by a multiple of the carrier frequency. Only products of trigonometric functions with equal frequency contribute a baseband term:

$$s_b(t) = I_0(b_c)I_0(b_s) - 2I_2(b_c)I_2(b_s) + 2I_4(b_c)I_4(b_s) - \ldots \tag{3.34}$$

Using this expansion in (3.31) and proceeding as in (3.29) yields

$$V_o(t) = V_T \ln\left(I_0(b_c)I_0(b_s) - 2I_2(b_c)I_2(b_s) + 2I_4(b_c)I_4(b_s) - \ldots\right) \tag{3.35}$$

This awkward expression is not very insightful, except for the fact that the inphase and quadrature components are combined in some complicated way and hence the noise will be modulated by the signal. As can be seen in Table 3.4, the expansion of the modified Bessel Functions of the first kind yields polynomials where the exponent of the first term increases with the function order. Thus it is valid to expand equation (3.35) into a two–dimensional Taylor Series to capture the important behavior of the inphase and quadrature components:

$$V_o = V_T \left(\frac{c^2}{4} + \frac{s^2}{4} - \frac{c^4}{64} - \frac{s^4}{64} - \frac{s^2c^2}{32} + \frac{c^6}{576} + \frac{s^6}{576} + \frac{c^2s^4}{192} + \frac{c^4s^2}{192} - \ldots \right) \tag{3.36}$$

This result is consistent with equation (3.30) for the case with only a modulated cosine–carrier applied to the envelope detector. The nonlinear behavior is mainly quadratic. Furthermore, the

terms up to fourth order stem exclusively from the product of the two zero–order modified Bessel–Functions, only the cross–term $\frac{c^2 s^2}{32}$ and higher order terms are due to higher order products. Both equations (3.35) and (3.36) can be easily implemented in a baseband equivalent simulation framework. The approximate power series representation (3.36) will result in a faster simulation time as special functions like the Bessel functions are normally computed using some recursive algorithm whereas the power series can be computed directly, resulting in fewer floating point operations. Because the higher order terms decrease rapidly and the main region of interest is for low input voltages, terms of order six and higher can be safely neglected in the implementation.

modified Bessel function	Taylor expansion
$I_0(x)$	$1 + \frac{x^2}{4} + \frac{x^4}{64} + \frac{x^6}{2304} + o(x^8)$
$I_1(x)$	$\frac{x}{2} + \frac{x^3}{16} + \frac{x^5}{384} + \frac{x^7}{18432} + o(x^9)$
$I_2(x)$	$\frac{x^2}{8} + \frac{x^4}{96} + \frac{x^6}{3072} + o(x^8)$
$I_4(x)$	$\frac{x^4}{384} + \frac{x^6}{7680} + o(x^8)$
$I_6(x)$	$\frac{x^6}{46080} + o(x^8)$

Table 3.4: Taylor Series Expansion of Modified Bessel Functions of the First Kind

3.6 Noise

Noise in a communication system is a construct used to encompass many different physical mechanisms that are impossible to model deterministically, either due to their inherent physical nature or to the complexity describing them. To completely specify the noise processes resulting from all sources one would need the joint probability distribution for any number of epochs. Significant simplifications can be obtained through further assumptions, notably due to the central limit theorem: many physical noise sources arise through the superposition of innumerable independent elementary processes, leading to a jointly Gaussian characteristic of the macroscopic process. Stationarity assumptions are often a very good approximation for the timescales of interest. A good summary of various noise sources in electronic circuits can be found in the book by Demir and Sangiovanni–Vincentelli [40]. To find the optimum detection rule for a communication system and to assess the performance in terms of the probability of error, it is theoretically possible to find a complete mathematical description of the system and compute the probability distribution functions necessary to obtain the likelihood ratio giving the optimum detection rule. But incomplete

specification of the noise processes and complicated noise transformations in nonlinear circuits render this approach infeasible in this case. A common technique in such cases is the Monte Carlo method: several time domain sample paths are generated by a random number generator[21] and the moments of the system output approximate the true stochastic characterization.

3.6.1 Thermal Noise

The classical result for the noise of any two–terminal device having resistance R independent of the geometry, material etc. was calculated by Nyquist to be a wide sense stationary Gaussian process with power spectral density $S_N(f) = \frac{2kT}{R}$ where T is the absolute temperature of the device and k Boltzmann's constant[22]. For the frequency range of interest, thermal noise can be modeled as white, although this is not physically meaningful for $f \rightarrow \infty$. At the receiver, the antenna as well as elements of the receiver chain contribute thermal noise. Thermal noise in the antenna is associated with its radiation resistance (typically 50Ω), which at the frequencies of interest dominates the noise contributed by the electromagnetic properties of the channel itself. Thermal noise in active MOS devices is associated with the channel resistance. Traditionally the effects of thermal noise are assessed by using a link budget analysis based on the Frijs equations as described by Rudell [41]. All linear components along the signal path are characterized by a noise figure relating the noise power at the output to the noise power at the input. However, this methodology is no longer valid for nonlinear subsystems in the signal path.

In the simulation framework here, I adopted the methodology described by Yee [4], associating a bandlimited white noise source with the antenna and relating the noise contribution of the first stage (the linear RF amplifier) back to the noise source. Assuming an input matched to the radiation resistance of 50Ω, the single sided PSD of the noise voltage is

$$R_n(\tau) = E\left[v_{in}(t)v_inT + \tau\right] = \frac{1}{2}kTR =: \frac{N_0}{2} \tag{3.37}$$

Hence with the convention for the baseband equivalent noise process described in the appendix, the power spectral density of the complex baseband equivalent process is $R_z(\tau) = 2N_0$. In RF design,

[21] The term 'pseudorandom' would be more appropriate here as all random number generators in simulation environments produce deterministic sequences with approximately the same stochastic characterization as the process to be simulated.

[22] $1.38 \times 10^{-23} J/K$

it is common to use the single sided power spectral density (describing the noise for physical frequencies $f \geq 0$), which is just twice the double–sided PSD, $4kTR$.

3.6.2 Flicker Noise

Flicker noise is the dominant noise process at low frequencies. The physical mechanism generating this noise process is still not completely agreed on in the literature. Important for the effects on receivers in MOS technology is the observation that the noise characteristics are in general nonstationary and not Gaussian. The variations are large even between devices on the same die and very dependent on the IC process employed. Several models for the simulation of flicker noise are proposed by Demir [40], but none of them is suitable to the problem at hand. This is mainly due to the fact that traditional circuit simulation tools only use frequency domain noise analysis, focusing on the effects of a linearized circuit model on a small additive white Gaussian noise signal. Hence device models only contain information for the (crude) approximation of flicker noise as a WSS Gaussian process passed through a filter with the characteristic $\frac{1}{\sqrt{f}}$ frequency response. Measurement results are not normally available across a large sample of devices from different dies to better characterize the noise statistics. Hence the model used in this simulation framework is limited to be of the same type, i.e. filtered white Gaussian noise. Dennis Yee developed a Flicker noise source [4] which can be readily used here after some minor modifications to allow frame–based processing. The parameters can be extracted from circuit simulation using the device models provided by the IC foundry, namely the flicker noise corner and the associated thermal noise level. The flicker noise source is inserted after the block modeling the nonlinear envelope detector transfer function, implicitly assuming that the flicker noise does not undergo the nonlinear transformation.

3.7 Demodulation and Detection

Demodulation and detection is the process of transforming the received continuous waveform into a stream of bits according to some decision rule. The goal is to minimize the probability of wrong decision. If the cost for a missed detection and a false detection is equal (as in the case at hand),

the maximum a posteriori rule (MAP) minimizes the overall as well as the component–wise probability of error. If the input symbols are equally likely, the MAP rule reduces to the maximum likelihood rule (ML). In a linear receiver in white Gaussian noise, the ML decision rule can be implemented using a matched filter and a simple threshold test for every symbol if the symbols are independent, i.e. there is no inter–symbol interference and no correlation introduced by means of coding. If the symbols are correlated, the optimal detector has to operate on the whole sequence of received symbols. A specific implementation of this maximum likelihood sequence detector is the well–known Viterbi algorithm. But the implementation complexity is high, rendering it infeasible for channels introducing severe inter–symbol interference. Suboptimal schemes referred to as equalizers are commonly used to mitigate inter–symbol interference.

The nonlinear nature of the proposed receiver and the non–Gaussian, non–white noise lead to a detection problem which is very difficult to analyze. As the statistics of the noise change with the signal level, the detector would need to be different for every channel state. To keep the problem simple and implementation complexity low, a Gaussian approximation can be used. This implies that higher order statistics are not taken advantage of while making a decision, which in turn means that not all available information is used and the detection is suboptimal. But the statistics of the noise are not well specified anyway, as described in the preceding section 3.6, hence the Gaussian approximation is the best possible strategy.

The nearly rectangular pulses will be distorted by the finite bandwidth filtering, hence inter–symbol interference is introduced, depending on the signal level. If equalization is to be performed, the equalizer has to adapt to the channel condition for every new packet, therefore training symbols are needed, incurring the penalty of additional overhead. This makes the equalization approach highly unattractive. The question is thus if a simple symbol–by–symbol threshold detector will perform well enough. For a very simple detector, several implementations are possible:

- An oversampling analog to digital converter, followed by a matched filter and a slicer is the standard approach. The oversampling A/D converter is energy–expensive, every extra bit increases the power consumption by a factor of four. On the other hand, well–established synchronization algorithms can be used.
- An all–analog implementation would consist of a gated integrator and a comparator (one

bit A/D converter). For approximately rectangular pulses, a gated integrator is the optimal receive filter in Gaussian noise. This implementation has the potential for very low power consumption. Synchronization of the integrator is important, but no schemes have been developed yet for this approach.

- A simple one bit A/D converter oversampled by a very high factor followed by a digital lowpass filter can also be implemented with low power consumption. As before, synchronization is not readily available.

For implementation in the simulation framework, additional constraints are given by the simulation speed. A matched filter running at the full simulation bandwidth would need 4000 taps for a symbol duration of $10^{-4}s$, making the simulation prohibitively slow. A compromise modeling the first two detectors described above is to downsample the incoming signal to some multiple of the symbol rate after it has been bandlimited by a lowpass filter and then use a windowed integrator as an approximation to a matched filter, followed by a slicer. Synchronization is implicit and adjusted up front for the optimal sampling instant. The windowed integrator approximates the analog integrator and is also a good model for the digital implementation of the matched filter because no multipliers would be needed, simplifying the digital implementation considerably.

3.8 Limitations

The simulation framework relies on several assumptions and simplification. Each of them introduces modeling errors and hence to interpret the simulation results correctly, these limitations have to be taken into account.

- Probably the single largest modeling error is due to the uncertainty in modeling the noise. Two main aspects need to be considered. The first is the inherent problem in accurately modeling the flicker noise process, i.e. generate a pseudo–random process that matches the statistical characteristics of the physical process. The second is to obtain the correct parameters to calibrate the model to match the specific circuit at hand. Neither of these two points is resolved completely satisfactory: The filtered Gaussian noise model is not very well

suited to describe a flicker noise process and the parameters used to characterize the actual devices are not very accurate. At the same time the noise has a major impact on the system performance, especially the noise introduced after the envelope detector stage. To obtain a better characterization of the device noise, measurements are the only way to verify the model used in the simulation.

- The modeling of the FBAR filters was a compromise to allow for a reasonable execution time. But to completely capture the characteristic of the filters, a larger bandwidth would be needed. A simulation bandwidth delimited by the wideband front–end filter, which has enough rejection to treat is as effectively bandlimited, would be desirable. The slow simulation speed though prohibits a larger simulation bandwidth.

- The power amplifier and the RF amplifier are treated as ideal linear components. Nonlinearities in the RF amplifier will be small compared to the envelope detector and for operation at the sensitivity limit of the receiver, the simple linear model is valid. however for very small separation of the receiver from the transmitter, the RF amplifier might overload and introduce sever distortion. The model presented does not capture this effect; instead it suggests a quasi–infinite dynamic range not limited for high inputs and hence is not useful to study the receiver performance in this regime.

  A good model for the power amplifier was difficult to obtain at the time of this writing because an all–new PA completely different from the first one is being designed[23] at the moment. The effects of the current PA are lumped into the waveform generation as described in section 3.2.1. Because the simulation model only performs linear amplification after the pulse–generation, the effect of a changing nonlinear behavior with signal amplitude is not captured. Simulation results showing a sweep in output power are effected by this problem. The new PA will operate in a highly nonlinear class C configuration and a new extraction of the transmitted pulse shapes will be necessary.

- The presented simulation framework captures a single point–to–point link in a noisy environment. However, it does not model the effect of in–band interferers nor close by blockers. This is in fact a crucial point not only for the simulation framework but also for the system under consideration. A major reason for using superheterodyne receivers is their very good

[23]PA design is done by Y.-H. Chee.

channelization performance due to the ease with which filtering at some intermediate frequency can be realized. Filtering at RF on the other hand is difficult. The micromachined filters used in this design are promising but their rejection is not sufficient yet. Thus it is important when comparing the performance of different architectures to take this fact into account and not claim energy savings which are actually due to insufficient RF filtering.

4 Simulation Results and Analysis

The simulation framework was used to assess key performance metrics for the proposed radio link. I performed several different experiments, the results of which are described in the following section. To include the effect of channel fading and to get a better understanding about the key parameters influencing the system behavior, a simplified model for manual analysis is described in section 4.2. This model is used to study the impact of channel fading in section 4.3.

4.1 Simulation Results

4.1.1 Data Rate and Transmit Power

The data rate is an important design parameter. To evaluate the rates possible and the transmit energy needed for a given probability of error, multiple simulations have to be performed. Figure 4.1 shows the results of these simulation runs. For different data rates, the path loss was varied to obtain the characteristic waterfall curves. This is equivalent to changing the transmitted power level. The duality is explored in the comparison of the two subgraphs. Figure 4.1.1 shows the impact of increasing the data rate while keeping the transmitted power constant (0dBm in this experiment). If the data rate is increased by a factor of two, the transmitted power also has to be increased by a factor of two to keep the transmitted energy per bit constant. This scenario is plotted in figure 4.1.1, where the same data set is normalized to yield a constant transmitted energy per bit. In a linear receiver all curves would overlap as the error probability depends only on the transmitted energy per bit. Because of the quadratic envelope detector characteristic, the received energy per bit in the proposed receiver is different from the transmitted energy, and hence a performance gain,

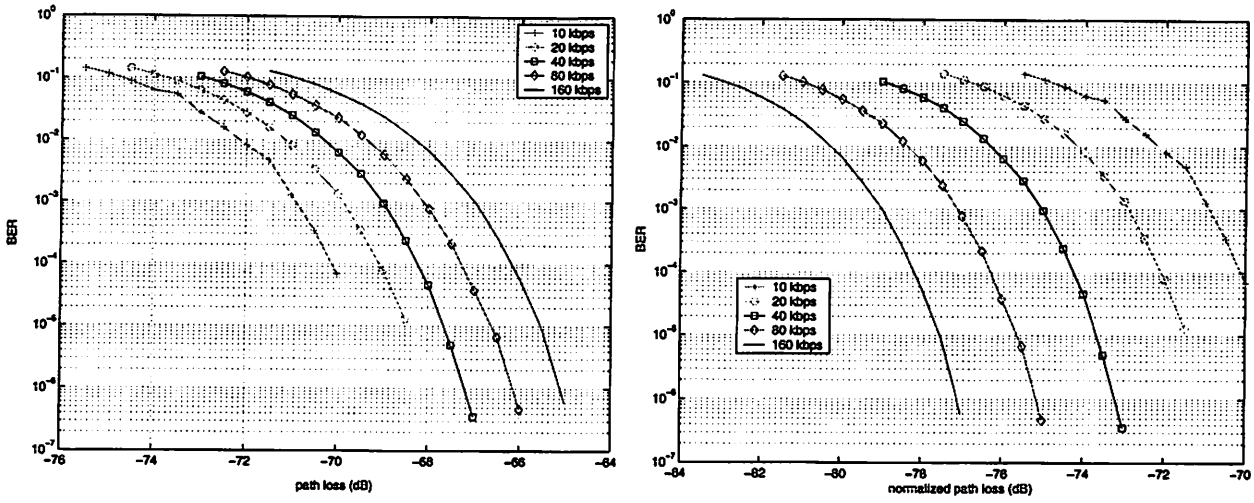

(a) 0 dBm Transmit Power

(b) Normalized Transmitted Energy per Bit

Figure 4.1: Error Probability for Different Data Rates

or equivalently a reduction in transmitted energy can be realized by increasing the data rate and the transmitted power. The received energy is linear in the symbol time while the it is quadratic in the transmitted power, hence to keep the error probability constant, a 1.5 dB ($\sqrt{2}$) reduction in transmitted energy per bit can be obtained for an increase in the data rate by a factor of two.

4.1.2 RF Amplifier Gain

There are two main noise sources in the system: thermal noise at the antenna and subsequent stages (matching network, RF amplifier) and flicker noise plus thermal noise at the envelope detector output. The RF amplification is important to overcome the effect of the baseband noise sources. To see which noise sources limit the performance of the system, two experiments are performed, one by varying the path loss of the channel and one by varying the gain of the RF amplifier. Simulations are performed at a data rate of 160 kcps[24] and 6 dBm transmit power. The results are shown in figure 4.2, where the overall path loss from the transmitter to the envelope detector input is plotted on the abscissa.

The two curves are indistinguishable, indicating that path loss and RF gain are quasi inter-

[24] *kcps* stands for kilochips per second, where a chip is the elementary modulation pulse, either **ON** or **OFF**.

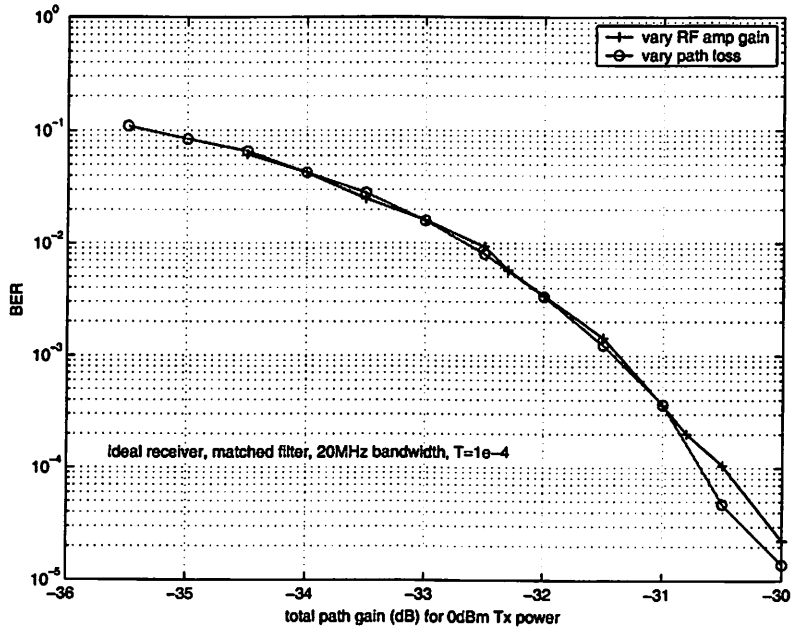

Figure 4.2: Effect of Variation in the Path Loss and Variation in the RF Amplifier Gain

changeable. The impact of a noise sources on the system performance is inversely proportional to the gain of the stage preceding the noise source. But no difference between the path loss (or the transmit power level) and the RF amplifier gain can be observed, hence the RF noise sources are negligible compared to the baseband noise sources. An ideal receiver should be designed such that all noise sources contribute equivalently to the overall system noise budget, which clearly is not the case for the design under investigation. A large amount of RF gain is needed to overcome the baseband noise, a severe drawback as high RF gain is difficult to achieve while keeping the power consumption of the amplifier low. Fortunately the noise figure of the RF amplifier is unimportant, hence a low power implementation might still be possible. Furthermore, RF gain can be interchanged for transmit power such that the power amplifier can be designed for the optimal efficiency.

4.1.3 Pulse Shape

The rise and fall time of the pulse is a design parameter since it is possible to modulate the oscillator bias current, resulting in different rise and fall times. The goal of this experiment was to evaluate if a performance benefit can be obtained from this scheme. The original pulse shape re-

sembles a rectangular pulse; hence the bandwidth is high and the relatively narrowband front–end and baseband filters will distort the pulse, introducing inter–symbol interference, which in turn may degrade the performance. Shaping the pulse by prolonging the rise and fall time reduces the bandwidth and maybe the inter–symbol interference while at the same time the energy contained in the pulse is reduced. For this simulation experiment, a chip rate of 160 kcps was used. Transmit power was fixed at 6dBm, path loss at -72.5dB. The pulse was assumed to be symmetric and the rise and fall times were modified by a factor multiplying the coefficients a and b in equation (3.2). Simulation results are shown in figure 4.3

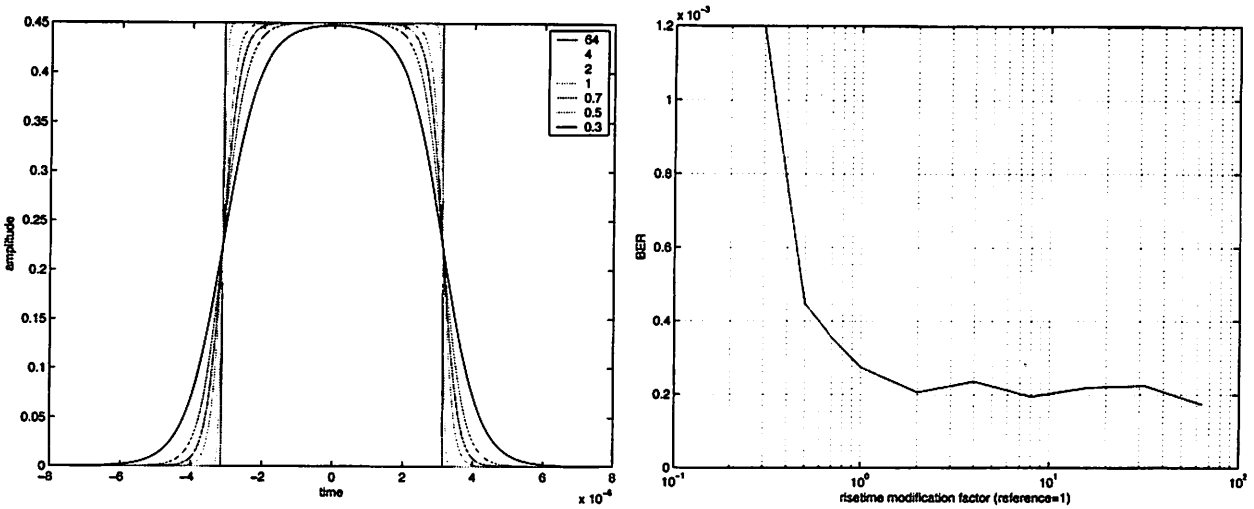

(a) Pulses used in the Experiment

(b) Bit Error Rate Simulated

Figure 4.3: Dependency of the Chip Error Rate on the Pulse Shape for a Chip Rate of 160 kcps

The reference pulse for a multiplier of one results from triggering the oscillator without modulating the bias current. Multipliers larger than one are hypothetical and only used for comparison, because the minimum rise time is fixed. A sharp increase in error rate can be observed for slower rise times than the reference whereas for the case of near rectangular pulses the error probability does not vary considerably. The fluctuation observed is below the simulation accuracy. Two factors are responsible for this degradation. A look at the eye–diagrams in figures 4.4–4.6 indicates that the shaped pulses actually contribute *more* inter–symbol interference than the lowpass filtered original pulse. Furthermore the total energy conveyed per pulse is reduced.

An important conclusion can be drawn from this results. Reducing the symbol time does not change the minimum risetime, which is set by the oscillator startup time. Hence the approximately

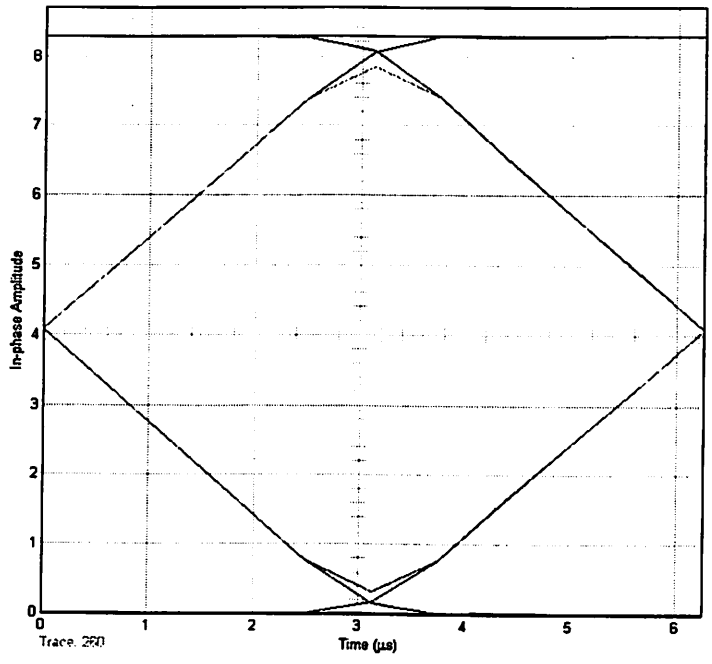

Figure 4.4: Eye Diagram for $a = 64$

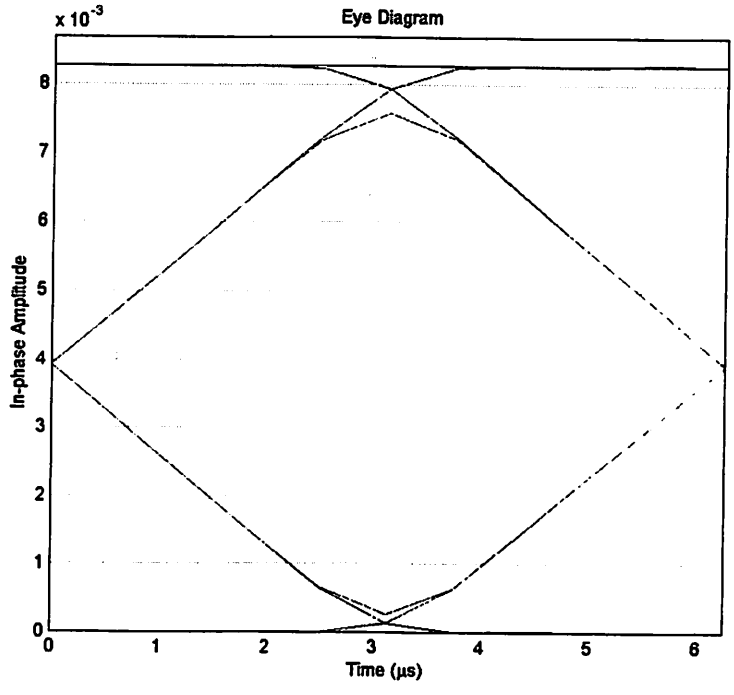

Figure 4.5: Eye Diagram for $a = 1$

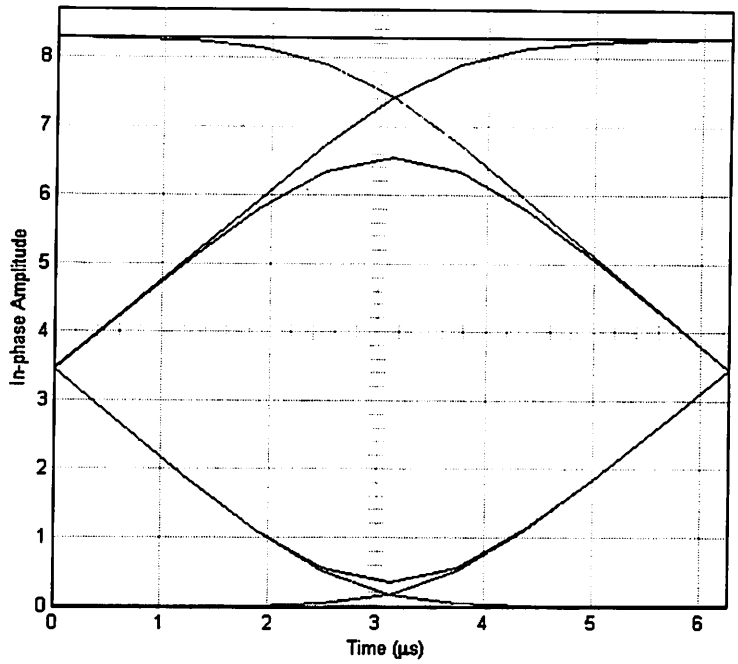

Figure 4.6: Eye Diagram for $a = 0.3$

rectangular pulse shape degrades for shorter symbols and at some point inter–symbol interference limits the performance. For the simulated symbol time of $6.25\mu s$ the pulse shape has already deviated significantly; a further reduction in symbol time has the same effect as changing the rise time for a constant symbol time. But figure 4.3 shows that for a further increase in risetime the error probability will increase. Hence 160 kcps is close to the upper limit of feasible chip rates.

This observation is also important for the choice of the modulation scheme. The fact that only an on–off-keyed signal is available limits the modulation scheme already to either *direct modulation*, where a logical **1** is modulated as an **ON** pulse and a logical **0** as an **OFF** pulse or *orthogonal modulation* where both logical levels are modulated as a sequence of chips, e.g. **ON–OFF** to signal a logical **1** and **OFF–ON** to signal a logical **0**. To maintain the same data rate, the orthogonal scheme needs a chip rate which is twice the chip rate for the direct modulation scheme. But the maximum chip rate is limited to 160 kcps and hence the orthogonal modulation scheme would only achieve a data rate of 80 kbps. The only advantage of the orthogonal modulation is an easier implementation of the detector: a simple implementation would just use a matched filter for both orthogonal symbols and compare them, selecting the hypothesis corresponding to the larger matched filter output, whereas for the direct modulation case, a threshold has to be defined which depends on the signal level and has to be estimated first. But this estimation can be performed in conjunction with the

timing synchronization, sharing the same pilot sequence.

4.2 A Simplified Analytical Model

The simulation results indicated a strong dependency of the non–faded performance on the envelope detector and the noise level at the detector output. To gain more insight, I derive a model suited for semi–manual analysis in the following section, explicitly showing the effect of the envelope detector transfer characteristic and the baseband noise. To arrive at a simple formulation, this model does not take into account the non–ideal pulses and filter characteristics.

All further derivations assume an ideal rectangular pulse at the transmitter and throughout the receiver chain. To achieve an output power level P_o at the transmitter into a 50Ω antenna, the power amplifier needs to produce a voltage swing of

$$\hat{V}_{o,TX} = \sqrt{2P_{o,TX}50\Omega} \tag{4.1}$$

where $\hat{V}_o$ denotes the voltage from zero to peak. The baseband equivalent envelope has the same magnitude[25]. Although the signal is radiated through space and picked up by the receiver antenna, the path loss G_{PL} can be modeled in terms of the voltage swing, assuming omnidirectional antennas without gain. Hence at the input of the RF amplifier, neglecting front–end filtering, the voltage level is

$$V_{in,RF} = V_{o,TX}G_{PL} = \sqrt{2P_{o,TX}50\Omega}G_{PL} \tag{4.2}$$

If the RF amplifier has gain G_{RF}, the signal level at its output is simply

$$V_{out,RF} = V_{in,RF}G_{RF} = V_{o,TX}G_{PL}G_{RF} \tag{4.3}$$

With the assumed ideal rectangular pulse, the nonlinearity of the envelope detector only alters the amplitude of the incoming signal:

$$V_{out,det}(V_{in}) = V_T \log\left[\mathrm{I}_0\left(\frac{V_{in}}{nV_T}\right)\right] \tag{4.4}$$

The envelope detector thus acts as an input dependent gain stage with gain

$$G_{det}(V_{in}) = \frac{V_{out,det}(V_{in})}{V_{in}} \tag{4.5}$$

[25]The definitions used in the baseband equivalent representation are summarized in appendix A.1

Putting the pieces together, the envelope amplitude at the output of the detector is

$$\begin{aligned} V_{out} &= V_{out,RF} G_{det}(V_{out,RF}) \\ &= V_{o,TX} G_{PL} G_{RF} \times G_{det}(V_{o,TX} G_{PL} G_{RF}) \end{aligned} \tag{4.6}$$

With the symbol time T, the average energy per received symbol can now be calculated as $\frac{1}{2}E_s = TV_{out}^2$, assuming equally distributed symbols. The notion of energy here is to be understood in a communication theoretic sense, as the energy delivered into a virtual 1Ω resistor.

The propagation of the noise through the receiver chain is somewhat more complicated. Noise is introduced by the equivalent radiation resistance of the antenna. The single–sided power spectral density of the baseband equivalent complex Gaussian noise process is $N_0 = 2kTR$, where k is Boltzman's constant, T the ambient temperature and R the antenna resistance, in this case 50Ω. The additional noise due to the RF amplifier is commonly described by the noise factor F [41]. Hence the noise PSD at the output of the RF amplifier is

$$N_{0,RF} = N_0 G_{RF}^2 F \tag{4.7}$$

Evaluating the effect of the envelope detector nonlinearity on the noise is complicated and in fact an exact calculation is not possible if the incoming noise process is not bandlimited[26]. Another approach is to view the noise as a small fluctuation around the mean, given by the signal amplitude, and then translate this fluctuation in frequency without changing its statistics. This is the way SPICE performs an AC noise analysis. In the low SNR regime this assumption might not hold, but as already observed in the simulation, the limiting factor is the noise added *after* the envelope detector, hence the linearization is valid. Stephens [14] claims that a squaring nonlinearity increases the noise power by $F_d = 2$ (3dB), but doesn't give a proof[27].

To capture the effect of the flicker noise at the envelope detector output, it also has to be

[26]This clearly is a modeling problem, as a physical noise process is always bandlimited, but for modeling simplicity, front–end filtering is omitted.

[27]Unfortunately I was not able to find a proof either, hence this number is quite arbitrary here. In fact the complete linearization mentioned above is strictly speaking not valid as it preserves the noise distribution whereas a quadratic nonlinearity always changes it. Just looking at the second moment, i.e. the noise power implies a Gaussian distribution. This in turn means that additional information available about the noise process is ignored, representing a worst case bound. But the input noise and the scaling factor don't have much influence on the overall system performance, hence for a quick analysis the approximations made are reasonable.

represented as some equivalent white Gaussian noise at a certain power level. Assuming simple symbol–by–symbol decisions at the slicer implies projecting the incoming signal plus noise onto a rectangular pulse (matched filtering). This is only a sufficient statistic if the noise is white, i.e. uncorrelated in all dimensions [42]. Otherwise information is lost and the detection is suboptimal. But as pointed out earlier, the flicker noise is neither Gaussian nor stationary, hence preprocessing the signal by a whitening filter is not an option. The noise variance at the input to the slicer can be back–annotated to yield the power of an equivalent white noise process that would result in the same probability of error for the symbol by symbol decisions. Obtaining this equivalent noise power is still difficult analytically as the integration of the $\frac{1}{f}$ spectrum is not finite — which again is clearly a modeling problem. The approach taken here is thus just a pure curve–fitting of the simplified model to the bit error rate curve obtained by simulation. The noise floor obtained from the device models was at $10^{-13}\frac{V^2}{Hz}$ with a flicker noise corner of 10kHz, hence the equivalent noise PSD should be of the same order, somewhat above the noise floor. In fact, the curves fit very well for 20 kcps chip rate with an equivalent detector noise of $N_d = 4.5 \times 10^{-13}\frac{V^2}{Hz}$. Using this number, the overall noise PSD at the envelope detector output is

$$N_{0,det} = F_d N_{0,RF} \times G_{det} \left(V_{o,TX} G_{PL} G_{RF}\right)^2 + N_d \tag{4.8}$$

The signal to noise ratio per bit can now be computed as

$$\begin{aligned}
\gamma_b =& \frac{E_s}{N_{0,det}} \\
=& \frac{T \left(V_{o,TX} G_{PL} G_{RF} \times G_{det} \left(V_{o,TX} G_{PL} G_{RF}\right)\right)^2}{2 \left(F_d N_{0,RF} \times G_{det} \left(V_{o,TX} G_{PL} G_{RF}\right)^2 + N_d\right)} \\
=& \frac{T V_{out,det} \left(V_{o,TX} G_{PL} G_{RF}\right)^2}{2 \left(F F_d N_0 \frac{V_{out,det} \left(V_{o,TX} G_{PL} G_{RF}\right)^2}{\left(V_{o,TX} G_{PL}\right)^2} + N_d\right)} \\
=& \frac{T}{2 \left(\frac{F F_d N_0}{\left(V_{o,TX} G_{PL}\right)^2} + \frac{N_d}{V_{out,det} \left(V_{o,TX} G_{PL} G_{RF}\right)^2}\right)}
\end{aligned} \tag{4.9}$$

And the probability of error for symbol–by–symbol decisions is given by means of the Q–function

$$P_e = \mathrm{Q}\left(\sqrt{\gamma_b}\right) \tag{4.10}$$

A comparison of the bit error rate obtained through simulation with the framework described above and the analytical model is shown in figure 4.7. The match is very good for the chip rate of 20 kcps,

where the fit of the equivalent baseband noise was performed. For different data rates, significant deviations can be observed. These curves don't deviate from the expected shape and a change in the fitting parameter N_d can align them perfectly with the simulated ones. The explanation thus has to focus on the increasing offset for higher data rates: the equivalent baseband noise spectral density models the effect of the flicker noise and the baseband thermal noise. With increasing data rate and thus increasing signal bandwidth, the noise power contributed by the flicker noise becomes less important as only a fraction of the overall signal bandwidth is affected by it. Therefore the model is not valid to predict the effect of different data rates but it is a good model for the effect of transmit power and path loss for a fixed data rate. This fact will be used to calculate the fading performance in the next section.

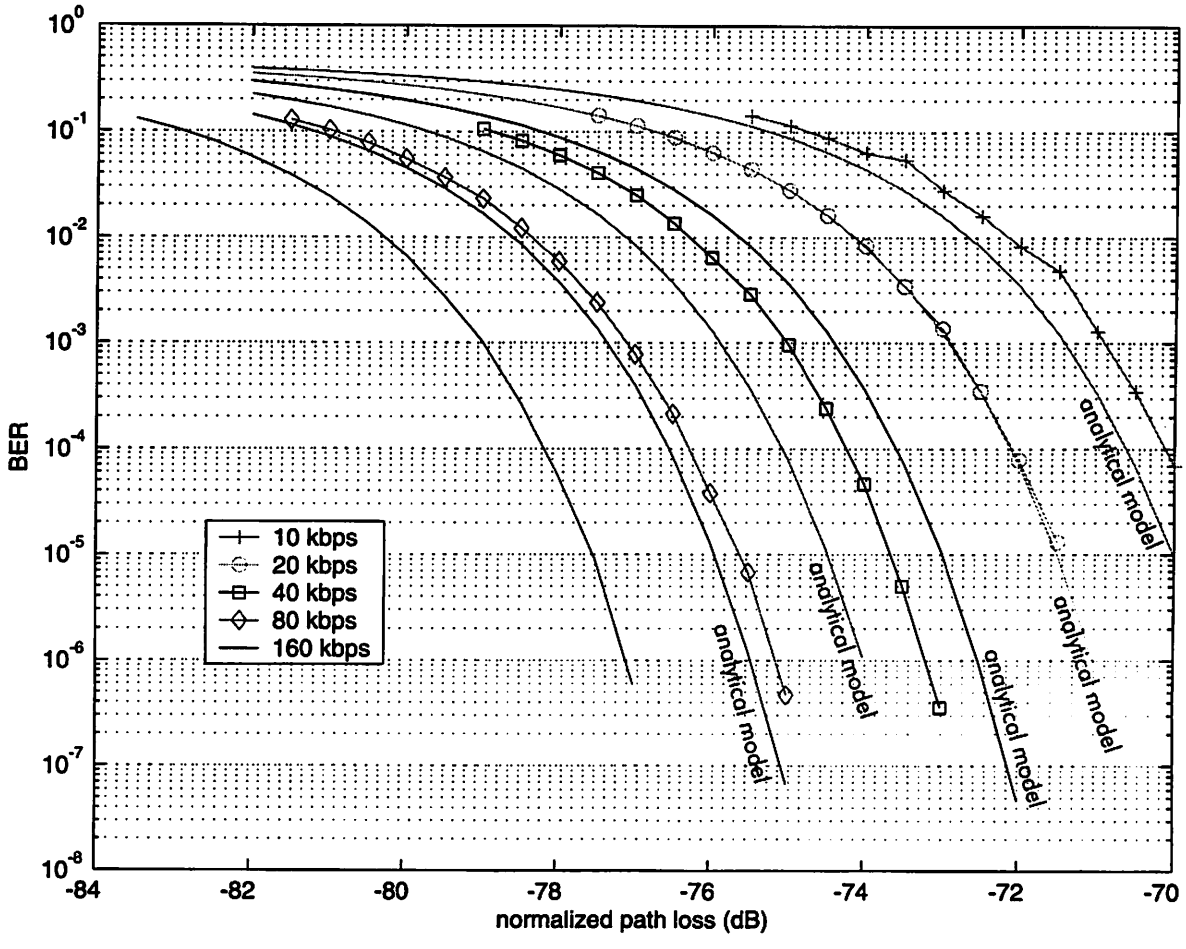

Figure 4.7: Comparison of Simulation and Analytical Model

The representation of the signal to noise ratio in equation (4.9) is reminiscent of the Frijs

equations, as the contribution of each noise source is dependent on the gain stage before the noise source. The relevance of the envelope detector gain characteristic can be appraised as it is quadratic in the input signal. An important observation is that the receiver performance is much more sensitive to the received signal power (and hence the received amplitude) than the pulse duration.

4.3 Effect of Fading

The dominant feature characterizing a wireless channel is *fading*, the variation of the channel over time. The main effect that induces channel fading is a dynamic variation in the length of the different propagation paths from transmitter to receiver. Constructive and destructive interference of these paths at the receiver causes the effective channel gain to vary. Whenever a path length changes on the order of a quarter wavelength, the interference pattern changes significantly. Indoor environments are characterized by a low relative mobility of transmitter, receiver and reflectors, hence the change in path length happens on the order of hundreds of milliseconds to seconds. In a discrete time model, the effects of fading can be captured by a multiplicative factor modifying the path loss. Several models exist for the statistics of these coefficients, the prevalent ones being the *Rayleigh* and the *Rician* distributions for the path magnitudes. The Rayleigh model is appropriate for a fully scattering environment where all propagation paths are reflected independently and arrive at the receiver from all directions. A scenario with a dominant path due to a line of sight between transmitter and receiver or a single strong reflected path is better modeled by the Rician distribution. Various measurements of indoor channels suggest that the Rician model is often a better description, even if there is no apparent line of sight [20] [29] [24].

To evaluate the effect of channel fading on the error performance of the system under consideration, the analytical model derived above can be used. The path loss coefficient has to be modified to include the fading coefficient magnitude: $G_{PL} \rightarrow |h|G_{PL}$. To obtain the new error probability, the Q–function has to be averaged over all possible fading states, $P_e = \mathrm{E}\left[Q\left(\sqrt{\gamma_b}\right)\right]$, where $\mathrm{E}[\cdot]$ denotes the expected value. The channel fluctuates around the large scale path loss, hence the power in the distribution of h has to be normalized to one. The Rayleigh distribution is then given by

$$f_{Rayleigh}(|h|) = 2|h|e^{-|h|^2} \tag{4.11}$$

The Rician fading model is characterized by the ratio of the power in the direct path versus the power in the specular paths. This ratio is commonly denoted the *k–factor*, defined as $k = \frac{\mu^2}{\sigma^2}$. The total power again has to be normalized; the resulting distribution function is

$$f_{Rician}(|h|) = 2(k+1)|h|e^{-\left(|h|^2-\frac{k}{k+1}\right)(k+1)} I_0\left(|h|\sqrt{4k(k+1)}\right) \tag{4.12}$$

Depending on the environment, typical values for the k–factor are between one (Rayleigh–fading) and six. Evaluation of the expectation is difficult. A numerical evaluation is plotted in figure 4.8 for the 10 kcps case.

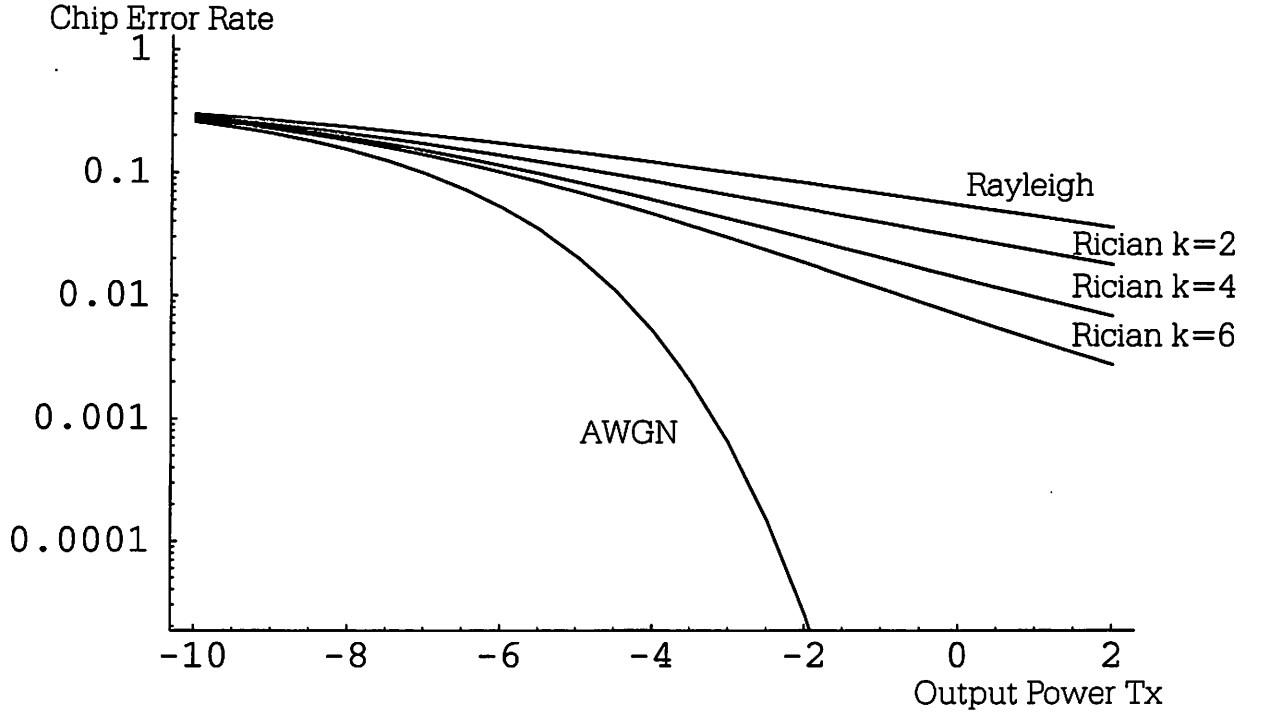

Figure 4.8: Faded vs. Non–faded Error Probability

The result is qualitatively the same as for a standard fading channel: the performance is very poor. A channel below the average occurs with high probability, leading to a sharp increase in error rate. A good channel on the other hand improves the error performance, but the average of both cases still yields a performance far inferior to the one of the unfaded channel. The simplest remedy — increasing the transmit power — is very costly as a 20dB increase is needed to obtain the target error performance of 10^{-4} for a non line of sight channel ($k = 2$), as can be observed in figure 4.9.

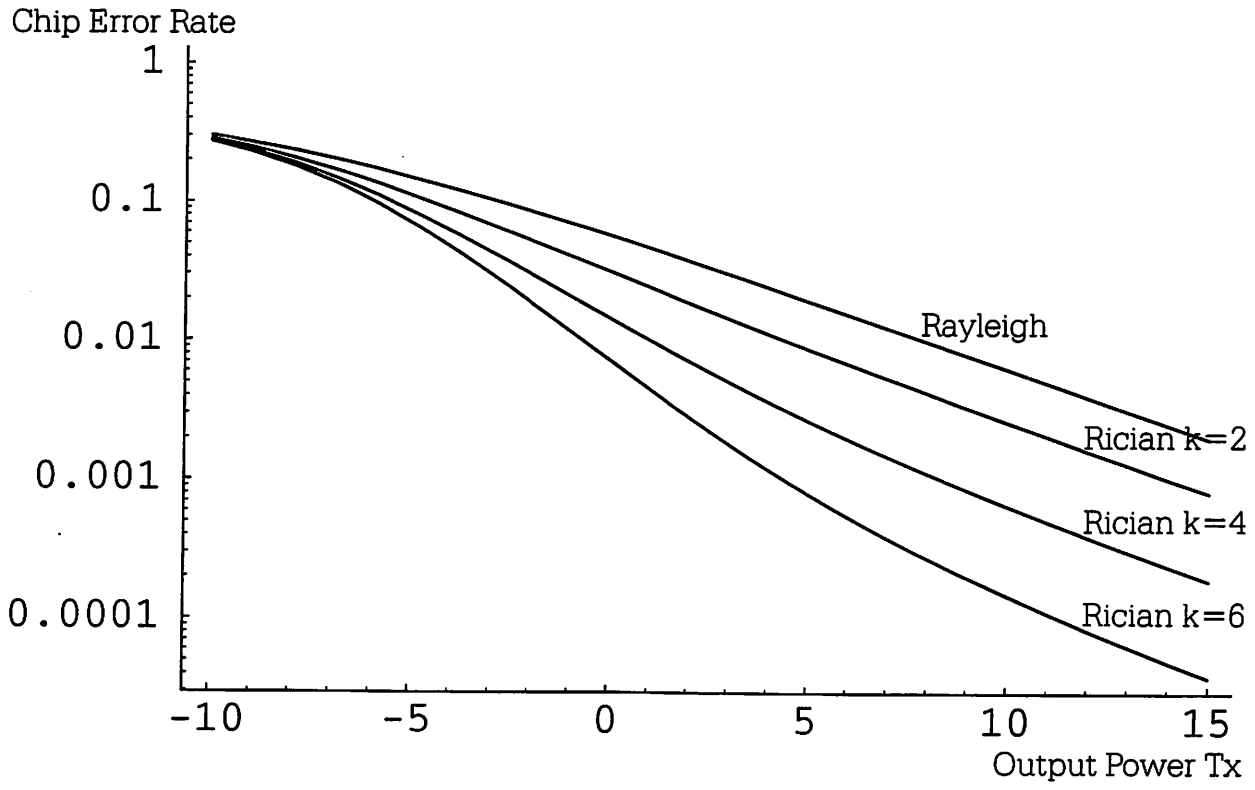

Figure 4.9: Rayleigh and Rician Fading Error Probability

To mitigate the effect of fading, diversity techniques have to be used. If several independently faded paths exist between the transmitter and the receiver, the probability that all of them will experience a deep fade at the same time is lower than for the single path case. Several standard diversity schemes exist and are examined next.

- *Time diversity* is achieved by spreading the information over a long time by means of coding and interleaving. The time used for interleaving has to be larger than the coherence time of the channel. This option is ill suited for the PicoRadio system. As described in section 3.3, the coherence time for indoor channels is quite long, hundreds of milliseconds and more. Conversely, the simulation results indicate that the packets should be kept short in order to return the radio to sleep mode fast, hence no time diversity can be harvested.

- *Spatial diversity* relies on the fact that signals transmitted or picked up by multiple antennas spaced sufficiently apart experience different channels. For a carrier frequency of 2 GHz, the spacing has to be at least a quarter wavelength, i.e. 3.75cm, which clearly is more than the form factor of the integrated PicoNode of $1cm^3$ allows for.

- *Frequency diversity* can be obtained by spreading the signal over a bandwidth larger than the coherence bandwidth of the channel. Independently faded replicas can then be combined using a *Rake* receiver. The system under consideration here is a narrowband system, hence no frequency diversity is available for a single channel. However, multiple channels spaced sufficiently far apart can be used with the transmitted signal coded across channels.

Because of the nature of a sensor node network, several other possibilities exist to provide diversity. A node normally sees several neighboring nodes that can help to achieve multiple paths and provide information about the channel quality. Two basic approaches are outlined below:

- If the channel state is known to the transmitter, an *opportunistic communication* strategy can be employed where the node only transmits when the channel is good. The basic assumption here is that the extra latency introduced while waiting for a good channel can be tolerated. A modified scheme can select the best channel among a set of channels to different nodes. This implies that several possible routes exist through the network. Hence network–level routing algorithms have to provide different alternative routes to choose from. The problem with all opportunistic schemes is the fact that the transmitter needs to have an estimate of the channel quality. To obtain this estimate, additional energy is required in the form of transmitting and receiving pilot signals.

- *Cooperative diversity* does not rely on channel quality estimates by always forwarding the data packets to multiple nodes. Laneman, Tse and Wornell explore different cooperative protocols for a single–hop transmission [43]. For a sensor node network, the ultimate goal is not just to provide a reliable point–to–point link but also to successfully transmit a packet from the source to the destination node. Therefore a scheme exploring cooperative diversity has to be designed on the level of the network layer, taking into account routing information.

To evaluate the performance of various diversity schemes, the energy consumption has to be taken into account. For comparison, the simple minded approach of increasing the transmitted power serves as an upper bound.

A Simplified Channel Model The simulation framework presented is only capable of estimating the probability of error for a fixed channel. Fading effects are not modeled and have to be included afterwards. For the design of the MAC and network layer, simpler models are needed to support the simulation of thousands of packets transmitted between multiple nodes. Because of the slow fading nature of the channel, it is a good assumption to model the channel as constant over the duration of a packet or even over the course of a data session including various acknowledge packets. Furthermore because of the sharp transition from a virtually error free channel to a channel causing a very high error rate, it seems valid to simply abstract the channel into two states, a *good* state with very low error probability and a *bad* state with high error probability. Depending on the time between successive transmissions, the occurrence of the states can be modeled as independent or correlated. The first case arises when transmissions occur at intervals spaced much further apart than the coherence time of the channel, i.e. on the order of seconds, whereas the second case is appropriate for transmissions only a coherence time apart. The simplest model for the second case introducing memory is a two–state Markov chain, similar to the Gilbert–Elliot model for bursty channels [17]

The probability of the good state and the bad state depends on the node separation and can be obtained by integrating over the tail of the Rician distribution multiplied by the average path loss for the corresponding distance given in equation (3.6). Depending on the chosen data rate and RF amplifier gain, a threshold can be defined separating the good and the bad SNR regime and delimiting the integration region.

5 Conclusions and Perspectives

The simulation framework presented addresses the need to better understand the effect of different building blocks in the analog transceiver chain of the PicoRadio wireless sensor network. The models derived for the individual blocks show a good fit with circuit simulation or measured data where available. The single most limiting factor is the modeling uncertainty for the flicker noise of the envelope detector. Simulation speed is still somewhat slow if the goal is to simulate a vast number of different parameter combinations, but it is sufficient to obtain the key performance results within reasonable time.

Simulation results indicate a very strong dependence of the bit error rate performance on the overall path loss and RF amplifier gain. Two main factors leading to this result can be identified: first, the nonlinear transfer characteristic of the envelope detector acts as input dependent gain stage with a quadratic gain function and second, the non–faded performance of the receiver is dominated by the flicker noise at baseband.

The quadratic nonlinearity also leads to the important conclusion that increasing the data rate is beneficial within certain limits, because only approximately 1.5 dB increase in transmit power is required to maintain the same energy per bit at the receiver while reducing the symbol time in half. At the same time the radio can be turned off twice as fast and the collision probability on the channel is decreased. The startup time of the oscillator limits the data rate to approximately 160 kbps using direct modulation. Not included in this analysis is the energy overhead due to the detection scheme used. A multi–bit analog to digital converter scales superlinearly with the data rate and must be taken into account in further investigations. Also not considered here are possible synchronization mechanisms. Symbol synchronization is necessary for every detection scheme; the complexity increases with increasing data rate and the overhead due to the synchronization preamble can be significant.

A simplified analytical model can be derived. This model correctly predicts the performance for a fixed symbol rate but is pessimistic in comparing different symbol rates because of the decreasing importance of the flicker noise for signals with increasing bandwidth. The effects of a fading channel can be evaluated by averaging over the possible channel gains. This would be nearly impossible to do using the simulation framework, but with the analytical model, numerical integration yields the corresponding BER–curves. As the main result of this model, due to the quadratic envelope detector gain characteristic and the short packet duration compared to typical coherence times of indoor channels, the system can be abstracted using a Gilbert–Elliot type channel model where the channel is described by only two states, either good or bad. This is a significant simplification especially important for the design of the MAC and network layers.

Channel fading causes a severe performance degradation and has to be mitigated. The techniques applicable are limited, but some interesting possibilities arise due to the nature of the sensor network. Diversity schemes on a network level are an interesting field for further research and will be necessary if a narrowband, low duty–cycle radio is used, where traditional diversity techniques

are not available.

The heuristic approach to reduce the overall energy per successfully transmitted bit is not yet empirically verified. The simulation framework described does not allow to make energy estimates besides in the conventional communication theoretic sense (energy transmitted over the channel). Power consumption of analog components depends strongly on the chosen topology and technology. Nevertheless a first order approximation might be feasible using more sophisticated models for the analog building blocks. For a given topology, parameterized models appear feasible in a way that by exchanging single blocks the effects on the system performance can be evaluated and comparisons of the power estimates are possible. The scope of this work was too limited to build a library including all these power–characterized model, but the approach seems to be promising for further research.

A Baseband Equivalent Representations

A.1 Baseband Equivalent Signal and Noise

A baseband equivalent model of communications systems, where the bandlimited part of the frequency spectrum containing the useful signal is shifted down to yield a lowpass signal, is normally used for analysis. Whereas this methodology is convenient for hand analysis, it is of uttermost importance for simulation purposes. Typical simulation environments operate in with discrete time steps, hence the sampling theorem dictates that the time step used must be smaller than half the shortest timescale in the system to be simulated. Even if the signal bandwidth is constrained to several kilohertz, the carrier frequency in the gigahertz range would lead to unacceptable simulation times. Several different notions of a baseband equivalent system exist in the literature, distinguished by a scaling factor of 2 [26] or $\sqrt{2}$ [44] in order to normalize the energy of the signal in the passband and bandpass domain. In the following, I adopt a notation proposed by Zhang and Miller [45] without scaling factors. The bandlimited passband signal with carrier frequency f_c is defined as

$$s(t) = x(t)\cos(2\pi f_c t) - y(t)\sin(2\pi f_c t) = \Re\left\{s_b(t)e^{j2\pi f_c t}\right\} \tag{A.1}$$

where $s_b(t)$ is the baseband equivalent signal defined as the complex envelope

$$s_b(t) = x(t) + jy(t) \tag{A.2}$$

The power of the baseband equivalent signal is thus twice the power of the bandpass signal, which is physically evident from the modulation by a sinusoid. Additive white Gaussian noise is added to the signal with double sided power spectral density

$$S_n(f) = \begin{cases} N_0/2 & |f \pm f_c| < W/2 \\ 0 & \text{elsewhere} \end{cases} \tag{A.3}$$

The passband noise process can be represented in the same way as the signal:

$$\begin{aligned} n(t) &= n_I(t)\cos(2\pi f_c t) - n_Q(t)\sin(2\pi f_c t) = \Re\left\{z(t)e^{j2\pi f_c t}\right\} \\ z(t) &= n_I(t) + jn_Q(t) \end{aligned} \tag{A.4}$$

The autocorrelation function of the bandpass process is defined:

$$\begin{aligned} R_{nn}(\tau) &= E\left[n(t)n(t+\tau)\right] \\ &= R_{n_I}(\tau)\cos\left(2\pi f_c \tau\right) \end{aligned} \tag{A.5}$$

as $R_{n_I}(\tau) = R_{n_Q}(\tau)$ and $R_{n_I n_Q}(\tau) = -R_{n_Q n_I}(\tau) = 0$ because the ideal bandpass white noise has a real and even power spectrum and thus the autocorrelation has to be an even function. Hence the PSD of $n_I(t)$ or $n_Q(t)$ respectively is

$$S_{n_I} = \begin{cases} N_0 & |f| < W/2 \\ 0 & \text{elsewhere} \end{cases} \tag{A.6}$$

Defining the autocorrelation function of the complex baseband noise process as

$$\begin{aligned} R_{zz}(\tau) &= E\left[z^*(t)z(t+\tau)\right] \\ &= 2R_{n_I n_I}(\tau) \end{aligned} \tag{A.7}$$

using the general definition for the autocorrelation function of a random process without a scaling factor, the PSD is thus

$$S_z(f) = \begin{cases} 2N_0 & |f| < W/2 \\ 0 & \text{elsewhere} \end{cases} \tag{A.8}$$

The total noise power in the passband domain in thus $\sigma_n^2 = 2\frac{N_0}{2}W = N_0 W$ and of the baseband equivalent system $\sigma_z^2 = 2N_0 W$. Hence the noise power as well as the signal power is doubled in the baseband equivalent representation, preserving the signal–to–noise ratio. This representation is convenient as only the true envelopes of the signals appear.

A.2 Ideal Integrator Transfer Function

In general, a baseband equivalent response of a linear system can be obtained through the method described by Proakis [26]: First, the frequency response is limited to positive frequencies, then a frequency shift is performed, moving the desired carrier frequency to the baseband. As only a small bandwidth around the carrier is of interest, this band is first isolated it with an ideal bandpass of bandwidth W given by $h_{bp}(t) = W\text{sinc}(Wt)\exp(j2\pi f_c t)$. The filtered unit step function $U(t)$

is thus

$$\begin{aligned}
&\int_{-\infty}^{\infty} W\,\mathrm{sinc}(W\tau)e^{j2\pi f_c\tau}U(t-\tau)d\tau \\
=&W\int_{-\infty}^{t}\frac{\sin(\pi W\tau)}{\pi W\tau}\left(cos(2\pi f_c\tau)+j\sin(2\pi f_c\tau)\right)d\tau \\
=&\int_{-\infty}^{t}\frac{1}{2\pi\tau}\left\{-\sin\left[(2f_c-W)\,\pi\tau\right]+\sin\left[(2f_c+W)\,\pi\tau\right]\right\}d\tau \\
&+\int_{-\infty}^{t}\frac{j}{2\pi\tau}\left\{cos\left[(2f_c-W)\,\pi\tau\right]-\cos\left[(2f_c+W)\,\pi\tau\right]\right\}d\tau \\
=&-\frac{1}{2}\int_{-\infty}^{t}\frac{\sin\left[(2f_c-W)\,\pi\tau\right]}{(2f_c-W)\,\pi\tau}(2f_c-W)\,d\tau+\frac{1}{2}\int_{-\infty}^{t}\frac{\sin\left[(2f_c+W)\,\pi\tau\right]}{(2f_c+W)\,\pi\tau}(2f_c+W)\,d\tau \\
&+\frac{j}{2}\int_{-\infty}^{t}\frac{\cos\left[(2f_c-W)\,\tau\right]}{(2f_c-W)\,\pi\tau}(2f_c-W)\,d\tau-\frac{j}{2}\int_{-\infty}^{t}\frac{\cos\left[(2f_c+W)\,\pi\tau\right]}{(2f_c+W)\,\pi\tau}(2f_c+W)\,d\tau
\end{aligned} \tag{A.9}$$

These integrals can be expressed in terms of the Sine Integral and Cosine Integral functions. The Sine Integral is defined as [34] [46]

$$\begin{aligned}
\mathrm{Si}(x)&=\int_0^x\frac{\sin(\xi)}{\xi}d\xi \\
\text{with}\quad \mathrm{Si}(-x)&=-\mathrm{Si}(x)
\end{aligned} \tag{A.10}$$

and thus

$$\int_{-\infty}^{t}\frac{\sin(a\xi)}{a\xi}d\xi=\frac{\pi}{2a}\mathrm{sign}(a)+\frac{1}{a}\mathrm{Si}(at) \tag{A.11}$$

The Cosine Integral is defined as [47]

$$\mathrm{Ci}(x)=\int_{-x}^{\infty}\frac{cos(\xi)}{\xi}d\xi=\int_0^x\frac{1-cos(\xi)}{\xi}d\xi-\ln(x)-\gamma \tag{A.12}$$

where γ is the Euler–Mascheroni–Constant.

The first term in equation (A.9) can thus be written as

$$-\frac{1}{2}\int_{-\infty}^{t}\frac{\sin\left[(2f_c-W)\,\pi\tau\right]}{(2f_c-W)\,\pi\tau}(2f_c-W)\,d\tau=-\frac{1}{4}-\frac{\mathrm{Si}\left((2f_c-W)\pi t\right)}{2\pi} \tag{A.13}$$

and the second term accordingly

$$\frac{1}{2}\int_{-\infty}^{t}\frac{\sin\left[(2f_c+W)\,\pi\tau\right]}{(2f_c+W)\,\pi\tau}(2f_c+W)\,d\tau=\frac{1}{4}+\frac{\mathrm{Si}\left((2f_c+W)\pi t\right)}{2\pi} \tag{A.14}$$

The third and fourth term cannot be evaluated directly. Instead I use the integral

$$\int_{-\infty}^{t}\frac{\cos(\xi)-1}{\xi}d\xi=Ci(-t)-\ln(-t) \tag{A.15}$$

Hence third term is

$$\begin{aligned}
&\frac{j}{2}\int_{-\infty}^{t}\frac{\cos\left[(2f_c-W)\,\pi\tau\right]}{(2f_c-W)\,\pi\tau}(2f_c-W)\,d\tau \\
=&\frac{j}{2\pi}\left[\int_{-\infty}^{(2f_c-W)\pi t}\frac{cos(u)-1}{u}\mathrm{du}+\int_{-\infty}^{(2f_c-W)\pi t}\frac{1}{u}\mathrm{du}\right] \\
=&\frac{j}{2\pi}\left[\mathrm{Ci}\left(-(2f_c-W)\pi t\right)-\ln\left(-(2f_c-W)\pi t\right)\right]+\frac{j}{2\pi}\int_{-\infty}^{(2f_c-W)\pi t}\frac{1}{u}\mathrm{du}
\end{aligned} \tag{A.16}$$

And for the fourth term

$$\begin{aligned}
&-\frac{j}{2}\int_{-\infty}^{t}\frac{\cos\left[(2f_c+W)\,\pi\tau\right]}{(2f_c+W)\,\pi\tau}(2f_c+W)\,d\tau \\
=&-\frac{j}{2\pi}\left[\int_{-\infty}^{(2f_c+W)\pi t}\frac{cos(u)-1}{u}\mathrm{du}+\int_{-\infty}^{(2f_c+W)\pi t}\frac{1}{u}\mathrm{du}\right] \\
=&-\frac{j}{2\pi}\left[\mathrm{Ci}\left(-(2f_c+W)\pi t\right)-\ln\left(-(2f_c+W)\pi t\right)\right]-\frac{j}{2\pi}\int_{-\infty}^{(2f_c+W)\pi t}\frac{1}{u}\mathrm{du}
\end{aligned} \tag{A.17}$$

Combining the first and second term yields

$$\frac{1}{2\pi}\left[\mathrm{Si}\left((2f_c+W)\pi t\right)-\mathrm{Si}\left((2f_c-W)\pi t\right)\right] \tag{A.18}$$

and for the third and fourth term

$$\begin{aligned}
&\frac{j}{2\pi}\left[\mathrm{Ci}\left(-(2f_c-W)\pi t\right)-\mathrm{Ci}\left(-(2f_c+W)\pi t\right)+\ln\left(\frac{2f_c+W}{2f_c-W}\right)\right]-\frac{j}{2\pi}\int_{(2f_c-W)\pi t}^{(2f_c+W)\pi t}\frac{1}{u}\mathrm{du} \\
=&\frac{j}{2\pi}\left[\mathrm{Ci}\left(-(2f_c-W)\pi t\right)-\mathrm{Ci}\left(-(2f_c+w)\pi t\right)+\ln\frac{2f_c+W}{2f_c-W}-\ln\frac{2f_c+W}{2f_c-W}\right] \\
=&\frac{j}{2\pi}\left[\mathrm{Ci}\left(-(2f_c-W)\pi t\right)-\mathrm{Ci}\left(-(2f_c+W)\pi t\right)\right]
\end{aligned} \tag{A.19}$$

The impulse response of the filtered unit step resulting in the spectrum of $Z_1(s)$ bandlimited around the carrier is

$$\begin{aligned}
h_1(t)=&\frac{1}{2\pi}\left[\mathrm{Si}\left((2f_c+W)\,\pi t\right)-\mathrm{Si}\left((2f_c-W)\,\pi t\right)\right] \\
&+\frac{j}{2\pi}\left[\mathrm{Ci}\left(-(2f_c-W)\,\pi t\right)-\mathrm{Ci}\left(-(2f_c+W)\,\pi t\right)\right]
\end{aligned} \tag{A.20}$$

To obtain a baseband equivalent representation, equation (A.20) has to be shifted to baseband by multiplying it with the complex exponential $e^{-2\pi f_c t}$. Subsequent sampling at $2W$ yields the discrete time representation suitable for implementation.

B Derivation of Fourier Expansions

B.1 Expansion of $e^{b\sin(\omega t)}$

I use the generating function for the Bessel function of the first kind as given by Poularikas [48]:

$$e^{\frac{1}{2}\psi\left(x-\frac{1}{x}\right)} = \sum_{n=-\infty}^{\infty} J_n(\psi)\, x^n \tag{B.21}$$

Setting $x = e^{j\omega t}$ and $\psi = \frac{b}{j}$,I obtain

$$e^{\frac{b}{2j}\left(e^{j\omega t}-e^{-j\omega t}\right)} = e^{b\sin(\omega t)} = \sum_{n=-\infty}^{\infty} J_n(-jb)\, e^{jn\omega t} \tag{B.22}$$

Using the identities $I_n(t) = j^{-n}J_n(jt)$ and $I_n(-t) = (-1)^n I_n(t)$, it follows

$$e^{b\sin(\omega t)} = \sum_{n=-\infty}^{\infty} j^n (-1)^n I_n(b) e^{jn\omega t} \tag{B.23}$$

This is the complex Fourier–Series representation. To convert it into a real Fourier–Series in $cos(\cdot)$ and $sin(\cdot)$, the relation

$$U_{c,n} = c_n + c_{-n} \qquad n > 0 \tag{B.24}$$

$$U_{s,n} = -j\,(c_{-n} - c_n) \qquad n > 0 \tag{B.25}$$

can be used with c_n the complex Fourier–Series coefficients and $U_{c,n}, U_{s,n}$ the coefficients of the sine and cosine terms in the real Fourier–Series respectively. For the cosine part, using the fact that $I_{-n}(b) = I_n(b)$ yields

$$\begin{aligned} U_{c,n} &= I_n(b)\left[j^n(-1)^n + j^{-n}(-1)^{-n}\right] \\ &= I_n(b)(-1)^n\left[j^n + j^{-n}\right] \\ &= I_n(b)(-1)^n 2\cos\left(\frac{n\pi}{2}\right) \\ &= \begin{cases} 0 & \text{if } n = 1,3,\ldots \\ 2(-1)^{\frac{n}{2}} I_n(b) & \text{if } n = 2,4,\ldots \end{cases} \end{aligned} \tag{B.26}$$

And for the sine part:

$$\begin{aligned} U_{s,n} &= -jI_n(b)\left[j^{-n}(-1)^{-n} - j^n(-1)^n\right] \\ &= jI_n(b)(-1)^n\left[j^n - j^{-n}\right] \\ &= -2jI_n(b)(-1)^n \sin\left(\frac{n\pi}{2}\right) \\ &= \begin{cases} 2(-1)^{\frac{n-1}{2}} I_n(b) & \text{if} \quad n = 1,3,\ldots \\ 0 & \text{if} \quad n = 2,4,\ldots \end{cases} \end{aligned} \tag{B.27}$$

Thus combining the parts, I obtain the complete real Fourier–Series expansion

$$e^{b\sin(\omega t)} = I_0(b) + 2I_1(b)\sin(\omega t) - 2I_2(b)\cos(2\omega t) - 2I_3(b)\sin(3\omega t) + 2I_4(b)\cos(4\omega t)\ldots \tag{B.28}$$

B.2 Expansion of $e^{b\cos(\omega t)}$

The methodology here is the same as before. Starting from the generating function (B.21), I substitute $x = je^{j\omega t}$ and $\psi = \frac{b}{j}$ to obtain

$$e^{\frac{b}{2}\left(e^{j\omega t} + e^{-j\omega t}\right)} = e^{b\cos(\omega t)} = j^n \sum_{n=-\infty}^{\infty} J_n(-jb)\, e^{jn\omega t} \tag{B.29}$$

Hence

$$e^{b\cos(\omega t)} = \sum_{n=-\infty}^{\infty} j^{2n}(-1)^n I_n(b) e^{jn\omega t} \tag{B.30}$$

The coefficients of the sine and cosine terms in the real Fourier–Series expansion can be computed as before, yielding

$$\begin{aligned} U_{c,n} &= I_n(b)\left[j^{2n}(-1)^n + j^{-2n}(-1)^{-n}\right] \\ &= 2I_n(b) \quad n = 1,2,\ldots \end{aligned} \tag{B.31}$$

And

$$\begin{aligned} U_{s,n} &= jI_n(b)\left[j^{2n}(-1)^n - j^{-2n}(-1)^{-n}\right] \\ &= 0 \end{aligned} \tag{B.32}$$

Hence the Fourier–Series expansion is

$$e^{b\cos(\omega t)} = I_0(b) + 2I_1(b)\cos(\omega t) + 2I_2(b)\cos(2\omega t) + 2I_3\cos(3\omega t) + \ldots \tag{B.33}$$

References

[1] J. Rabaey *et al.*, "Picoradios for wireless sensor networks: the next challenge in ultra-low-power design," in *2002 International Solid-State Circuits Conference Digest of Technical Papers*, vol. 1. IEEE, Feb.3-7 2002, pp. 200–201.

[2] A.-S. Porret, T. Melly, D. Python, C. C. Enz, and E. A. Vittoz, "An ultralow–power UHF transceiver integrated in a standard digital CMOS process: Architecture and receiver," *IEEE Transactions on Systems Science and Cybernetics*, vol. 36, no. 3, pp. 452–466, Mar. 2001.

[3] L. E. Larson, "Radio frequency integrated circuit technology for low–power wireless communications," *IEEE Personal Communications Magazine*, vol. 5, no. 3, pp. 11–19, June 1998.

[4] D. G.-W. Yee, "A design methodology for highly-integrated low-power receivers for wireless communications," Ph.D. dissertation, University of California at Berkeley, Department of Electrical Engineering and Computer Science, Berkeley, CA, 2001.

[5] I. O'Donnell, M. Chen, S. Wang, and R. W. Brodersen, "Ultra–wideband transceiver prototype," in *BWRC Summer Research Retreat.* Lake Tahoe, CA: University of California at Berkeley, Department of Electrical Engineering and Computer Science, June2-4 2002.

[6] J. C. Haartsen and S. Mattison, "Bluetooth — a new low–power radio interface providing short–range connectivity," *Proceedings of the IEEE*, vol. 88, no. 10, pp. 1651–1661, Oct. 2000.

[7] V. Aparin, E. Zeisel, and P. Gazzerro, "Highly linear SiGe BiCMOS LNA and mixer for cellular CDMA/AMPS applications," in *2002 IEEE Radio Frequency Integrated Circuits (RFIC) Symposium. Digest of Papers.* Piscataway, NJ: IEEE, 2002, pp. 129–132.

[8] P. T. van Zeijl, J.-W. Eikenbroek, P.-P. Vervoort, S. Setty, J. Tangenberg, G. Shipton, E. Kooistra, I. Keekstra, and D. Belot, "A bluetooth radio in $0.18\mu m$ CMOS," in *2002 IEEE International Solid-State Circuits Conference. Digest of Technical Papers.* Piscataway, NJ: IEEE, Feb. 2002, pp. 86–87.

[9] G. Chang, L. Jansson, K. Wang, J. Grilo, R. Montemayor, C. Hull, M. Lane, A. Estrada, M. Anderson, I. Galton, and S. Kishore, "A direct conversion single–chip radio–modem for

bluetooth," in *2002 IEEE International Solid-State Circuits Conference. Digest of Technical Papers*. Piscataway, NJ: IEEE, Feb. 2002, pp. 88–89.

[10] J. Chea, E.-H. Kwek, E. C. Low, C. K. Quek, C. Yong, R. Enright, J. Hirbawi, A. Lee, H. Xie, L. Wei, L. Luong, J. Pan, S.-T. Yang, W. F. A. Lau, and W.-L. Ngai, "Design of a low–cost integrated $0.25\mu m$ CMOS bluetooth SOC in $16.5mm^2$ silicon area," in *2002 IEEE International Solid-State Circuits Conference. Digest of Technical Papers*. Piscataway, NJ: IEEE, Feb. 2002, pp. 90–91.

[11] F. Beffa, R. Vogt, W. Bächtold, E. Zellweger, and U. Lott, "A 6.5 mW receiver front–end for bluetooth in $0.18\mu m$ CMOS," in *2002 IEEE Radio Frequency Integrated Circuits (RFIC) Symposium. Digest of Papers*. Piscataway, NJ: IEEE, 2002, pp. 391–394.

[12] H. Meyr, M. Moeneclaey, and S. A. Fechtel, *Digital Communication Receivers*. New York, NY: John Wiley & Sons, 1998.

[13] B. P. Otis and J. M. Rabaey, "A $300\mu W$ 1.9GHz oscillator utilizing micromachined resonators," in *Proceedings of the* 28^{th} *European Solid–State Circuit Conference*, A. Baschirotto and P. Malcovati, Eds., vol. 28, IEEE. Fierenze, Italy: University of Bologna, Sept. 2002, pp. 151–154.

[14] D. R. Stephens, *Phase-Locked Loops for Wireless Communications*. Boston, MA: Kluwer Academic Publishers, 1998.

[15] B. P. Otis and R. Bocock, "Downconversion subsampling of RF signals," University of California at Berkeley, Department of Electrical Engineering and Computer Science," EECS 247 Term Project, Dec. 2000.

[16] D. M. Akos, M. Stockmaster, J. B. Y. Tsui, and J. Caschera, "Direct bandpass sampling of multiple distinct RF signals," *IEEE Transactions on Communications*, vol. 47, no. 7, pp. 983–988, July 1999.

[17] M. C. Jeruchim, P. Balaban, and K. S. Shanmugan, *Simulation of Communication Systems*, 2nd ed. New York, NY: Kluwer Academic Publishers / Plenum Publishers, 2000.

[18] R. N. Bracewell, *The Fourier Transform and Its Applications*, 2nd ed. New York, NY: McGraw–Hill, 1978.

[19] T. S. Rappaport, *Wireless Communications – Principles and Practices*, 2nd ed. Upper Saddle River, NJ: Prentice Hall, 2002.

[20] H. Hashemi, "The indoor radio propagation channel," *Proceedings of the IEEE*, vol. 81, no. 7, pp. 943–968, July 1993.

[21] I. Cuiñas and M. G. Sánchez, "Furniture effects on the wideband indoor radio channel at microwave frequencies," *Microwave and Optical Technology Letters*, vol. 29, no. 5, pp. 336–340, June 2001.

[22] *Propagation data and prediction methods for the planning of indoor radiocommunication systems and radio local area networks in the frequency range 900 MHz to 100 GHz*, International Telecommunication Union Recommendation ITU–R P.1238-2, Rev. 2.

[23] N. Patwari, Y. Wang, and R. J. O'Dea, "The importance of the multipoint–to–multipoint indoor radio channel in ad hoc networks," in *Proc. IEEE Wireless Communications and Networking Conference*, vol. 2. IEEE, 2002, pp. 608–612.

[24] D. Courivaud, C. Humbert, and M. Sylvain, "2 GHz single–floor indoor propagation results," in *Proc. IEEE International Conference on Trends in Communications (EUROCON'2001)*, vol. 2. IEEE, 2001, pp. 309–311.

[25] D. N. Tse, "Lecture notes for EE 290S, fundamentals of wireless communications," Fall 2002, University of California at Berkeley, Department of Electrical Engineering and Computer Science.

[26] J. G. Proakis, *Digital Communications*, 4th ed. New York, NY: McGraw Hill, 2000.

[27] H. Zepernick and T. Wysocki, "Multipath channel parameters for the indoor radio at 2.4 GHz ISM band," in *Proc. IEEE 49th Vehicular Technology Conference*, vol. 1. IEEE, 1999, pp. 190–193.

[28] K. Kurek, D. Janusek, and T. Kosilo, "Characteristic of the indoor propagation channel in 1.9 GHz band," in *Proc. IEEE 13th International Conference on Microwaves, Radar and Wireless Communications (MIKON)*, vol. 2. IEEE, 2000, pp. 383–386.

[29] S.-C. Kim, H. L. Bertoni, and M. Stern, "Pulse propagation characteristics, at 2.4 GHz inside buildings," *IEEE Transactions on Vehicular Technology*, vol. 45, no. 3, pp. 579–592, Aug. 1996.

[30] R. C. Ruby, P. Bradley, Y. Oshmyansky, and A. Chien, "Thin film bulk wave acoustic resonators (FBAR) for wireless applications," in *Proc. 2001 IEEE Ultrasonics Symposium*, vol. 1. Piscataway, NJ: IEEE, 2001, pp. 813–821.

[31] R. C. Ruby, P. Bradley, J. Larson III, Y. Oshmyansky, and D. Figueredo, "Ultra–miniature high–Q filters and duplexers using FBAR technology," in *ISSCC 2001: IEEE International Solid-State Circuits Conference Digest of Technical Papers*. Piscataway, NJ: IEEE, Feb. 2001, pp. 120–121.

[32] J. D. Larson III, P. D. Bradley, S. Wartenburg, and R. C. Ruby, "Modified Butterworth–Van Dyke circuit for FBAR resonators and automated measurement system," in *Proc. IEEE Ultrasonics Symposium 2000*, vol. 1. Piscataway, NJ: IEEE, 2000, pp. 863–868.

[33] A. V. Oppenheim, R. W. Schafer, and J. R. Buck, *Discrete–Time Signal Processing*, 2nd ed. Upper Saddle River, NJ: Prentice Hall, 1998.

[34] H.-D. Lüke, *Signalübertragung*, 7th ed. Berlin: Springer, 1999.

[35] S. Venkatesh, "Lecture notes on envelope detection," 1999, EE414/EE530 - Introduction to Statistical Communications, University of Pennsylvania.

[36] R. G. Meyer, "Low-power monolithic RF peak detector analysis," *IEEE Journal of Solid-State Circuits*, vol. 30, pp. 65–67, Jan. 1995.

[37] ——, "Lecture notes for EE242 — advanced integrated circuits for communications," Fall Semester 2002, University of California at Berkeley, Department of Electrical Engineering and Computer Science.

[38] T. Serrano-Gotarredona, B. Linares-Barranco, and A. G. Andreou, "A general subthreshold MOS translinear theorem," in *Proceedings of the 1999 IEEE International Symposium on Circuits and Systems VLSI*, vol. 2. Piscataway, NJ: IEEE, 1999, pp. 302–305.

[39] R. G. Meyer, "Lecture notes for EE142 — integrated circuits for communications," Spring Semester 2002, University of California at Berkeley, Department of Electrical Engineering and Computer Science.

[40] A. Demir and A. Sangiovanni-Vincentelli, *Analysis and Simulation of Noise in nonlinear electronic Circuits and Systems*. Boston, MA: Kluwer Academic Publishers, 1998.

[41] J. C. Rudell *et al.*, "An integrated GSM/DECT receiver : design specifications," University of California at Berkeley, Department of Electrical Engineering and Computer Science/Electronics Research Lab, Berkeley, CA, UCB ERL Memorandum UCB/ERL M97/82, Apr. 1998.

[42] D. N. Tse, "Lecture notes for EE224 — digital communications," Spring Semester 2002, University of California at Berkeley, Department of Electrical Engineering and Computer Science.

[43] J. N. Laneman, D. N. Tse, and G. W. Wornell, "Cooperative diversity in wireless networks: Efficient protocols and outage behavior," *submitted to IEEE Transactions on Information Theory*, Jan. 2002.

[44] E. A. Lee and D. G. Messerschmitt, *Digital Communication*, 2nd ed. Boston, MA: Kluwer Academic Publishers, 1994.

[45] W. Zhang and M. J. Miller, "Baseband equivalents in digital communication system simulation," *IEEE Transactions on Education*, vol. 35, no. 4, pp. 376–382, Nov. 1992.

[46] I.N.Bronstein, K. Semendjajew, G.Musiol, and H. Mühlig, *Taschenbuch der Mathematik*, 3rd ed. Frankfurt am Main: Verlag Harri Deutsch, 1997.

[47] E. W. Weisstein, "The cosine integral," in *Eric Weisstein's World of Mathematics*. Wolfram Research Inc. [Online]. Available: http://mathworld.wolfram.com/CosineIntegral.html

[48] A. D. Poularikas, *The Handbook of Formulas and Tables for Signal Processing*. Boca Raton, Fl: CRC Press & IEEE Press, 1999.